Chromatin arranges in filaments of blobs with nanoscale functional zonation

E. Miron[1,5], R. Oldenkamp[1,5], D. M. S. Pinto[2], J. M. Brown[3], A. R. Faria[1], H. A. Shaban[4], J. D. P. Rhodes[1], C. Innocent[1,6], S. de Ornellas[3], V. Buckle[3], L. Schermelleh[1,2]*

[1] Department of Biochemistry, University of Oxford, Oxford OX1 3QU, United Kingdom

[2] Micron Oxford Advanced Bioimaging Unit, University of Oxford, Oxford OX1 3QU, United Kingdom

[3] MRC Weatherall Institute of Molecular Medicine, Haematology Unit, University of Oxford, Oxford OX3 9DS, United Kingdom

[4] Spectroscopy Department, Physics Division, National Research Centre, 12622 Dokki, Cairo, Egypt

[5] Current address: Division of gene regulation, Netherlands Cancer Institute, Plesmanlaan 121, 1066 CX Amsterdam, the Netherlands

[6] Current address: Neurology Department, Harvard Medical School, Boston Children's Hospital, 300 Longwood Ave, Boston MA 02115

*Correspondence should be addressed to L.S. (lothar.schermelleh@bioch.ox.ac.uk)

Keywords: Chromatin, TAD, epigenome, nuclear organization, quantitative image analysis, super-resolution microscopy, structured illumination microscopy, 3D-SIM

Three-dimensional (3D) chromatin organisation plays a key role in regulating genome function in higher eukaryotes. Despite recognition that the genome partitions into ~1Mb-sized topological associated domains (TADs) based on ensemble Hi-C measurements, many features of the physical organisation at the single cell level remain underexplored. Using 3D super-resolution microscopy, we reveal a sequential curvilinear arrangement of globular chromatin domains with viscoelastic properties ('blobs') juxtaposed to an RNA-populated interchromatin (IC) network. Quantitative mapping of genome function markers uncovers a zonal distribution, with RNA-binding factors concentrated in the IC, confinement of structural proteins and transcriptionally active/permissive marks to chromatin domain surfaces, and enrichment of repressive marks towards the interior. This correlation between nanoscale topology and genome function is relaxed in postreplicative chromatin, accentuated in replicative senescence, persists upon ATP depletion and hyperosmolarity induced chromatin condensation and, remarkably, after inactivation of cohesin. Our findings support a model of a higher-order chromatin architecture on the size level of TADs that creates and modulates distinct functional environments through a combination of biophysical parameters such as density and ATP-driven processes such as replication and transcription, but independent of cohesin.

The genome in mammalian cell nuclei is hierarchically organised at various size scales that correlate with diverse genomic functions[1,2]. At the base pair to kilobase pair level, DNA is wrapped around core histones to create nucleosomes that form the building blocks of chromatin[3]. At the 100 Mb scale, whole chromosomes harbour distinct territories within the nucleus with transcriptionally active euchromatic and inactive heterochromatic segments tending to segregate into specific nuclear sub-regions[4]. The intermediate chromatin organization ranging from several kb to 100 Mb still remains poorly understood[5]. Advances in next-generation sequencing based chromosome conformation capturing methods (3C/Hi-C) have revealed a genomic landscape composed of ~400 kb to ~1 Mb-sized topologically associating domains (TADs)[6,7]. TADs are genomic regions which have elevated intra-TAD interaction relative to sequences outside TADs; deletion of TAD boundaries leads to aberrant reprogramming of the transcriptome[8]. Chromatin immunoprecipitation sequencing (ChIP-Seq) identified the CCCTC-binding factor (CTCF) as a key regulator in TAD organisation, binding to convergently oriented recognition sequences which flank TADs and thus define their boundaries at the linear scale[9]. Although the exact mechanisms of TAD formation and maintenance has yet to be elucidated, co-occurrence of the ring-shaped

57 cohesin complex at CTCF binding sites suggest a regulatory role of cohesin in shaping TAD
58 structures through chromatin loop extrusion[10–13]. Accordingly, loss of cohesin function leads
59 to an erasure of TAD signatures on Hi-C interaction maps[14].
60 Whereas the linear genomic size of TAD structures is well defined, their
61 spatiotemporal organization is largely underexplored. Genomic-based methods such as Hi-C
62 and ChIP-Seq are characterized by the need for averaging large cell populations to generate
63 *in silico* models, thereby falling short in explaining the biophysical forces that maintain the 3D
64 epigenome. Ensemble data result in semi-quantitative models that do not address cell to cell
65 variability and lack information on the absolute structure and temporal dynamics of
66 chromatin domains. In fact, single-cell Hi-C and more recent microscopy-based approaches
67 observe variability in chromatin folding at the level of TAD topologies, highlighting a high
68 degree of stochasticity and heterogeneity in chromatin conformations *in situ*[15–18]. Fluorescent
69 *in situ* hybridization (FISH) of specific DNA regions has been a powerful tool in visualizing
70 chromatin structures, revealing the appearance of TAD topologies as chromatin domains
71 with a diameter of several hundred nanometres when imaged with super-resolution
72 microscopy[17,19–21]. *In silico* simulations of chromatin as a melted polymer suggest that the
73 charged properties of modified histone tails alter the compaction status of such chromatin
74 domains[22], thereby explaining the increase in physical size of epigenetically active domains
75 compared to epigenetically inactive domains[23]. It is further suggested that protein mobility is
76 hampered with increasing chromatin density through physical hindrance, which may allow
77 relative size differences between small transcription factors (TFs) and large nuclear macro-
78 complexes such as the transcription machinery to be exploited as a mechanism of
79 transcriptional control[24].
80
81 **3D super-resolution chromatin imaging reveals a curvilinear filament of coherently**
82 **moving globular domains, distinct from an RNA-occupied interchromatin network**
83 The study of <1 Mb chromatin domain topologies in single cells *in situ* and *in vivo* have long
84 been under-characterized in conventional microscopy studies, as their scales fall just beyond
85 the diffraction limit of light. Advances in super-resolution microscopy now put such structures
86 within spatial reach[17,21]. Super-resolution 3D structured illumination microscopy (3D-SIM)
87 enables fast multicolour 3D acquisition of whole cells with 8-fold enhanced volumetric
88 resolution and strongly enhanced contrast compared to conventional fluorescence
89 microscopy[25]. Previous 3D-SIM studies resolved 4′,6-diamidino-2-phenylindole (DAPI)-
90 stained chromatin in mammalian somatic cells as an intricate sponge-like structure, that is
91 juxtaposed to channels of no detectable chromatin (the inter-chromatin compartment, IC)

92 which permeate throughout the nucleus, ending at nuclear pores[26–28]. Using data quality-
93 controlled 3D-SIM (Methods; Extended Data Fig. 1a), we first confirmed the presence of this
94 structural arrangement in mouse (C127) and human (Hela) somatic cell lines (Extended
95 Data Fig. 1a-c). DNA staining with either DAPI or SYTOX Green after formaldehyde fixation
96 revealed the same characteristic pattern of a convoluted filamentous chromatin structure and
97 an interchromatin network (Extended Data Fig. 1b, left). Complementary 3D stimulated
98 emission depletion (STED) microscopy of SYTOX-labelled C127 cells confirmed the
99 topological features observed with 3D-SIM (Extended Data Fig. 1b, middle). Control
100 experiments in HeLa cells stably expressing histone H2B-GFP showed a near, albeit not
101 complete colocalisation of H2B-GFP and DNA staining, in line with a mixture of tagged and
102 untagged H2B incorporated into chromatin[29] (Extended Data Fig. 1c).
103 To better understand the nature of the seemingly 'empty' IC network compartment
104 we performed an extended 5-ethenyluridine (EU) pulse labelling and subsequent click
105 chemistry to detect all RNAs transcribed during the labelling period[30]. We observed a striking
106 enrichment of bulk RNA in the IC space including nucleoli and nuclear pore channels, and
107 almost mutual exclusion with DAPI-stained chromatin (Fig. 1a, b). Plotting a line profile
108 through a representative region of euchromatin shows RNA-filled IC and chromatin features
109 with minimal diameter of approx. 160 nm (Fig. 1c) up to several hundred nanometres in
110 heterochromatic regions (data not shown).
111 Along with a visual comparison we applied an unbiased non-linear segmentation
112 algorithm on the chromatin staining assigning each voxel in the nuclear space to one of
113 seven relative intensity classes with the lowest (class 1) denoting the IC, and the other
114 classes 2-7 denoting the chromatin compartment from low to high density (Methods,
115 Extended Data Fig. 1d). Of the quantified nuclear volume (Extended Data Fig. 1e) ~30%
116 was classified as IC network with subsequent decreasing proportions for lower to higher
117 chromatin density (classes 2 to 7, Extended Data Fig. 1d). We further assessed the average
118 diameter of the convoluted filamentous chromatin structure in C127 cells to be 350 nm
119 (Extended Data Fig. 3, Methods); the value is proximate to the mid-point (330 nm) of the
120 previous empirically observed ranges (Fig. 1c). To exclude fixation artefacts, we adopted our
121 3D-SIM acquisition scheme to enable fast live cell imaging of H2B-GFP expressing cells
122 confirming the presence of a chromatin – interchromatin network *in vivo* (Extended Data
123 Fig.1b, right). Time-lapse 3D-SIM imaging of HeLa H2B-GFP cells unveiled a highly dynamic
124 behaviour of chromatin domain features over different observation periods and time intervals
125 (Fig.1d, Extended Data Fig. 2a, Supplementary Movies 1-3).

126 Quantitative flow field analysis[31] (Methods; Fig. 1d, e; Supplementary Movie 4)
127 reveals spatially coherent motion of chromatin (i.e. fields with same motion direction) with a
128 correlation length of ~2.5 to 3 μm for time intervals between 2 s and >20 s, indicating a
129 change in correlation length of 0.5 μm between adjacent coherently moving domains (Fig.
130 1e, middle). This is accompanied by smoother transitions between these domains for
131 increasing time intervals (Fig. 1e, bottom). Mapping of chromatin dynamics by tracking flow
132 fields followed by Bayesian model selection demonstrates heterogeneity of chromatin motion
133 with sub-diffusive and super-diffusive dynamic regimes (Extended Data Fig. 2b). These
134 results are consistent with viscoelastic properties of chromatin characterised by mechanical
135 coupling and coherent motion of high-viscous droplet-like domains[31,32], best described as
136 diffusive 'blobs'.
137 Next, we used DNA fluorescence *in situ* hybridization (FISH) detection to place the
138 observed 3D chromatin landscape in the context of TADs as defined by Hi-C experiments.
139 Conventional DNA-FISH protocols require heat denaturation which disrupts chromatin
140 structures below ~1-Mb-size levels[33]. To overcome this potential problem, we have
141 implemented a non-denaturing FISH method, termed resolution after single-stranded
142 exonuclease resection (RASER)-FISH[34], in order to faithfully preserve chromatin
143 ultrastructure. We applied RASER-FISH to study the topology of a previously characterized
144 TAD (0.7 Mb TAD H) located on the mouse X chromosome[19] (Fig. 1f, Extended Data Fig.
145 4a). Quantitative analysis of 21 TAD H RASER-FISH signals from active (non-Barr body) X
146 chromosomes revealed an average core diameter of 350 nm. Although most TADs in single
147 cells display a globular shape they are not uniform spheres but extend in at least one
148 dimension to a maximum extension of 500 nm as confirmed by a standard deviation
149 between all TADs (Fig. 1g, Extended Data Fig. 4b). Importantly, TAD FISH signals coincide
150 with the underlying chromatin density stained by DAPI (Fig. 1f). Furthermore, multi-colour
151 RASER-FISH of neighbouring domains spanning the α-globin locus revealed a curvilinear
152 path, where each domain is a discrete blob within the convoluted filament (Fig. 1h, Extended
153 Data Fig. 4c).
154 We conclude that chromatin in somatic interphase cells arranges as a convoluted
155 curvilinear filament partitioned into discrete globular or extended chromatin blobs. These can
156 accommodate TADs in a range of chromatin densities and form physical viscoelastic entities
157 with constrained local dynamics that are separated from a DNA-free, RNA-occupied
158 interchromatin network space.
159
160

161

162 **Functional marker distribution reveal nanoscale 3D zonation**

163 Previous studies correlating Hi-C-based TAD distributions with ChIP-seq mapping of histone
164 post translational modifications (PTMs) and chromatin factors along the linear (1D) genome
165 highlighted an enrichment for cohesin and CTCF at the TAD boundaries[7]. Drawing from our
166 own previous study of non-random localization of active and silenced chromatin histone
167 PTMs[27,28], we undertook to systematically map genomic function against the observed
168 chromatin blob filament – IC network. To this end we have devised a pipeline (Cha*i*N, Chain
169 high-throughput analysis of the *in situ* Nucleome), Extended Data Fig. 5 and Methods for
170 details) for automated high-throughput image analysis, that allows mining spatial high-
171 content information from thousands of multicolour-labelled 3D-SIM nuclear volume datasets
172 after applying SIM optimized immunofluorescence (IF) labelling protocols[36] (Methods).
173 Cha*i*N classifies the chromatin signal into class 1 if no signal detected (the IC), classes 2 and
174 3 confined to the outer fringes of the blob filament, classes 4 and 5 denote the interior of
175 blobs and classes 6 and 7 primarily denoting densely packed constitutive heterochromatin
176 regions[28]. (Fig. 2a). We characterised the 3D epigenome landscape using 16 markers
177 (nascent RNA, RNA-associated proteins, chromatin-associated proteins and histone PTMs;
178 Fig. 2b, Extended Data Fig. 6a) in mouse C127 cells in G1 with 40 3D datasets from 2
179 biological repeats for each marker, each with hundreds to several thousands of annotated IF
180 foci (Extended Data Table 1).

181 First, we noted that RNA processing/interacting factors hnRNPC1/2, SAF-A
182 (hnRNPU), RNAP-S2P and nascent RNA transcripts are enriched in the IC class 1 and the
183 lowest chromatin classes 2 and 3, while they are depleted in the internalized chromatin
184 classes 4 and 5 and are virtually absent in the highest classes 6 and 7 (Fig. 2b, left).
185 Interestingly, those factors known to interact with chromatin, RNAPII-S2P, nascent RNA and
186 SAF-A, show a peak of enrichment in class 2, while the sole factor that only binds RNA,
187 hnRNPC1/2 shows the strongest enrichment in class 1. Accordingly, average nearest-
188 distance measurements to segmented chromatin boundary result in a mean distance
189 location of hnRNPC1/2 outside of chromatin, while the other three markers centre at the
190 segmented boundary (Fig. 2c, right). These results are in accordance with early immuno-EM
191 observations[37] that active transcription is confined to 'peri-chromatin' at the interface of
192 chromatin domains and the IC. They are also in line with the reported function of SAF-A as
193 an interactor of chromatin-associated RNAs[38] and support the concept of a physical 3D
194 interface between an RNA environment and decondensed outer fringes of chromatin blobs.

195 Unlike RNA-interacting proteins, the location distribution of segmented histone PTMs,
196 which are inherently chromatin-associated, show a marked depletion in the lowest intensity
197 class 1, thus validating those annotated voxels as a true interchromatin (IC) compartment.
198 Importantly, we observe a biased enrichment for both H3K4me3, typically located at
199 promoters of active genes, and H3K36me3, typically enriched along the body of transcribed
200 genes (Fig. 2b, left), in the lowest chromatin intensity classes 2 and 3 marking the outer
201 fringe region of the filament, with peak enrichment in class 2 similar to RNAPII-S2P and
202 nascent transcripts. These markers are rarely found in the higher intensity classes 4 and 5,
203 that denote the interior of blobs, and are almost absent in the classes 6 and 7, that mark
204 mainly constitutive heterochromatin (Fig. 2b, left). Their corresponding di-methylated forms
205 (H3K4me2 and H3K36me2), as well as acetylated H4K5, which has been implicated in
206 epigenetic bookmarking[39] also show a notable albeit less distinct enrichment in the lower
207 class range (peak in class 3) and depletion in higher classes.
208 In contrast, repressive histone PTMs generally show a broader distribution that is
209 shifted towards the higher intensity classes. The H3K27me3 mark, which is typically
210 deposited along Polycomb-mediated silenced genes[40] shows an enrichment in the interior
211 classes (3-5 peaking at class 4). H3K9me3, a marker for transcriptionally inactive facultative
212 and constitutive heterochromatin[40], is found enriched in the interior and heterochromatin
213 classes (3-7) but most abundant in heterochromatin classes (5-7, peak at class 6).
214 H4K20me3, which has been implicated in silencing repetitive DNA (e.g. in chromocenters of
215 mouse cells) and transposons[41] is most strongly enriched in the heterochromatin classes (6
216 and 7). Again, the di-methylated state H3K9me2 shows a notably less shifted distribution
217 than H3K9me3 peaking at the interior classes (class 4), similar to H3K27me3.
218 The distribution of CTCF and two sub-units of the cohesin complex Smc3 and Scc1,
219 was characterised by distinct enrichment in surface classes (1-2) and a depletion in the
220 higher classes as well as their distance profile centring at the segmented boundary of the
221 filament (Fig. 2b).
222 The observed differential enrichment of functional markers can also be considered in
223 light of the specific enzyme complexes responsible for their deposition. Indeed, there is a
224 remarkable inverse correlation, with smaller complex sizes correlating to peak enrichment in
225 higher chromatin classes of the corresponding marker (Fig. 2c), thus supporting the
226 hypothesis that chromatin density acts as a higher-level regulator of genome function by
227 hindering physical accessibility of larger complexes to substrate chromatin[24]. Analysing a
228 subset of markers in human colon (HCT116) and cervical (HeLa) cancer G1 cells, we found
229 highly similar characteristics of differential spatial distributions, confirming the universal

230 nature of the observed zonation (Extended Data Fig. 6b, c). Moreover, we restricted the
231 analysis to volumes of major euchromatic and heterochromatic regions, also denoted as
232 >10 Mb sized A and B compartments in Hi-C experiments. We sub-divided the nuclear
233 volume into lamina-associated chromatin plus chromocentre regions versus the residual
234 nuclear volume as proxy for B and A compartmentalization, respectively. We find the
235 nanoscale zonation true for both euchromatic A regions as well as heterochromatic B
236 regions (Fig. 2d, Extended Data Fig. 6d), highlighting the fact that both large-scale
237 compartments harbour transcriptionally active and inactive sequences, albeit at different
238 ratios[42] (Extended Data Fig. 6e) deviating from previous models of wholly active 'open' vs
239 inactive 'closed' domains.
240 In conclusion our high-content 3D super-resolution Cha*i*N mapping approach
241 highlights a nanoscale zonation of the chromatin filament topology with markers of active
242 transcription and architectural proteins being confined to the surface of the filament blobs
243 and silencing modification being enriched towards the interior, while the IC harbours most
244 RNAs and RNA interacting proteins. The increasing densities of nucleosomes from the
245 surface towards the interior of these blobs may lead to the physical exclusion (or hindrance)
246 of chromatin-associated complexes relative to their size, such that functional zonation is a
247 consequence of accessibility[24].
248
249 **The local topological landscape is temporarily relaxed during DNA replication and**
250 **consolidated in replicative senescence**
251 To assess the impact of DNA replication, we identified S-phase cells by short EdU pulse
252 labelling and grouped them into early, mid and late S-phase stages according to
253 characteristic replicon foci distribution pattern[43] before subjecting them to Cha*i*N analysis.
254 Taking the entire nuclear volume into account, no significant changes of marker distributions
255 could be seen in mouse C127 cells (Extended Data Fig. 7a), with the notable exceptions of
256 Scc1 and H4K20me3 (discussed below). To study whether replication impinges on its direct
257 local environment, we generated an EdU sub-mask of the nucleus that encompasses active
258 replication sites and post-replicative chromatin (Fig. 3a). Overlaying this sub-mask with the
259 segmented chromatin landscape reveals a strong decompaction indicating locally confined
260 disruption, likely caused by activity of the replication machinery. This is most dramatically
261 highlighted by tunnel-like voids becoming apparent in otherwise dense chromocentres in late
262 S-phase (Fig. 3b). Accordingly, EdU labelled replicon foci show an enrichment in the lower
263 chromatin density classes, irrespective of S-phase stage (Fig. 3c).

264 When quantifying chromatin classes and functional marker distribution in replicating
265 sub-regions, we observed expectedly a shift towards denser chromatin classes when
266 progressing from early, to mid, to late S-phase (Fig. 3d), and a highest abundancy of the
267 active histone PTM H3K4me3 in early S as compared to the repressive PTM H3K27me3,
268 which was most enriched in mid S phase (Fig. 3e, Extended Data Fig. 7b). Interestingly, the
269 depletion of Scc1 with increasing chromatin density as seen in G1 cells is noticeably
270 mitigated in S phase cells, already for the entire nuclear volume as well as in post-replicative
271 chromatin sub-volumes (Extended Data Fig. 7a, b) indicating an internalisation of cohesin
272 when acting in sister chromatid cohesion. Constitutive heterochromatin mark H4K20me3, on
273 the other hand, becomes less enriched in denser chromatin classes during late S-phase
274 (Extended Data Fig. 7a) with the opening of condensed chromatin. Restricting the analysis
275 to the EdU sub-mask shows a reduced enrichment in higher chromatin classes more so for
276 all repressive histone modifications than for active modifications through S-phase
277 progression (Extended Data Fig. 7b).
278 Since active replication temporarily opens dense chromatin and relaxes functional
279 marker distribution, we anticipated that replicative senescence (RS) would have the contrary
280 effect. To test this, we applied our ChaiN workflow to human IMR-90 cells comparing cycling
281 cells in G1 versus senescent RS cells. Indeed, the chromatin landscape in senescent cells
282 reveals a clear tendency to cluster into senescence-associated heterochromatin foci
283 (SAHFs, Extended Data Fig. 7c). Furthermore, we observed a substantial accentuation of
284 the spatial segregation of active and repressive functional markers in non-cycling cells
285 (Extended Data Fig. 7d).
286 Our data shows that active DNA replication can locally disrupt both the physical
287 organisation of chromatin and the functional zonation. As replication ceases, a profound
288 stabilisation of functional and structural compartmentalisation may lead to a 'transcriptional
289 lock-in' of gene expression profiles in senescent or terminally differentiated cells.
290
291 **Biophysical and biochemical perturbations affect 3D chromatin landscape**
292 To better understand the forces and potential mechanisms shaping the observed landscape
293 we next analysed various chemical and biophysical perturbations: (1) transcriptional
294 inhibition using triptolide, a potent inhibitor of RNAPI and RNAPII initiation, (2) reversible
295 induction of hypercondensed chromatin (HCC) by hyperosmolarity-mediated increase of
296 bivalent cations[44], and (3) ATP-depletion through irreversibly blocking of the respiratory
297 chain upon sodium azide (NaN_3) treatment[45]. Chromatin compaction becomes apparent
298 upon ATP depletion and is most prominent in hyperosmolarity induced hypercondensed

299 chromatin with finer filamentous features merging into larger, more compacted features and
300 concurrent widening of the IC (Fig. 4a). Accordingly, when quantifying parameters of the
301 segmented filament we observed an increasing shift of relative voxel number towards higher
302 intensity classes, while the overall volume ratio between IC class 1 and chromatin classes 2-
303 7 remain constant (Fig. 4c). More strikingly, however, the segmented chromatin surface area
304 to volume ratios (SA:vol) challenged by both hyper-osmotic or triptolide exposure decreases
305 significantly compared to G1 (Fig. 4d) and quantitatively underpin the changes in chromatin
306 observed by 3D-SIM imaging. Concomitantly, we observe a subtle but noticeable increase in
307 volume occupied by the perichromatin classes 2-3 (Fig. 4c), suggesting that transcription
308 initiation acts to constrain the perichromatin volume.
309 Analysing the spatial distribution of selected markers did not reveal any major
310 change in trend of distribution (Fig. 4b, Extended Data Fig. 8a). We did note an accentuation
311 of elongating RNAPII-S2P, and active transcription histone PTM H3K4me3 accumulating in
312 the surface classes (2-3) as progression from NaN_3 to HCC concomitant with Scc1 and
313 H3K4me3 being even more strongly depleted in the interior and heterochromatin classes (4-
314 7). There is a comparable marked reduction in distribution bias for both repressive histone
315 PTMs (H3K27me3 and H3K9me3) in both NaN_3 and HCC relative to G1, which is also
316 visible in Trip treatment for H3K27me3 but not for H3K9me3. Trip treatment generally
317 lessens depletion for all active markers in the interior and heterochromatin classes (4-7). We
318 see no change in the trend of average marker distances to the segmented chromatin-IC
319 boundary with only Scc1, CTCF and H3K27me3 showing a non-significant move away from
320 the chromatin/IC interface in Trip treatment (and NaN_3 to a lesser magnitude, Extended Data
321 Fig. 8b). Of note, the positioning of RNAPII-S2P remains stable around the segmented
322 chromatin-IC boundary in all analysed perturbations suggesting the underlying biological
323 demarcation of this surface is coupled to elongating transcription. The absolute numbers of
324 detected RNAPII-S2P signals are unchanged in both NaN_3 and HCC relative to G1
325 (Extended Data Table 1), indicating that elongating RNAPII remains attached to filament
326 surface regions regardless of chromatin being biophysically challenged; the numbers do
327 decrease to one third of those in G1 when transcription initiation is inhibited. For HCC the
328 lack of increased distance to the surface for repressive PTMs when there are increased
329 volumes of denser chromatin shows that repression via histone remodelling is limited to a
330 40-120 nm depth from the surface. It may be that the hindrance imposed from nucleosome
331 density is sufficient to avoid activation of promoters beyond this depth further supporting *in*
332 *silico* modelling of nucleosome melts[46].

333 Together the data shows that overall 3D zonation is unchanged by large-scale
334 rearrangements of the chromatin blob filament through chemical and biophysical forces,
335 even though different perturbations may induce subtle changes for individual markers.
336
337 **Cohesin function is dispensable for 3D chromatin structure and functional zonation**
338 To test the role of cohesin in maintenance of a TAD-harbouring chromatin filament and the
339 spatial segregation of the 3D epigenome we ablated the SCC1 (RAD21) subunit of the
340 cohesin complex in human HCT116 cells using auxin inducible protease degradation[47]
341 (Extended Data Fig. 9a-c). Upon addition of both doxycycline and auxin, Scc1 can be
342 depleted with a half-life of 17 min[47] to be completely ablated in 2 h (Extended Data Fig. 9d,
343 e). Strikingly, quantitative analysis of HCT116 wild type versus SCC1-mAID cells 6 h after
344 induction does not show any observable change in the chromatin filament structure (Fig. 5a-
345 c) or the absolute deposition of functional histone PTMs on this landscape (Fig. 5d,
346 Extended Data Fig. 9f-h). The chromatin filament diameter and relative chromatin surface
347 area to its volume does not change suggesting that suggesting cohesin is dispensable for
348 these structures.
349 Cohesin inactivation results in the complete elimination of TADs in Hi-C experiments
350 in HCT116 cells[14]. Our findings therefore demonstrate that loss of cohesin, and thereby
351 TADs, has no observable effect on higher-order structures. We conclude that cohesin and
352 TADs are not vital for maintaining the filament of blobs and are therefore also dispensable
353 for nanoscale functional zonation. We postulate that the role of cohesin is to guide relevant
354 physiological genomic loci to occupy the appropriate zonation generated from the physical
355 properties of chromatinised DNA *in situ*.
356
357 **Discussion**
358 Our novel high-throughput quantitation reveals that chromatin in somatic interphase cells
359 arranges as a curvilinear filament of sequential discrete chromatin blobs with local
360 viscoelastic dynamic properties and ordered densities that can harbour individual TADs. This
361 filamentous chain-like structure is separated from an RNA-rich interchromatin (IC) network
362 and the transition between these environments encompasses a defined nanoscale zonation
363 of genome functions relative to chromatin density, where active transcription and
364 architectural proteins are confined to the surface area and silencing marks are enriched
365 towards the interior of the nucleosomal entities (Fig. 6a). We show that the principle of 3D
366 zonation is unchanged by large-scale rearrangements of the filament through chemical and
367 biophysical forces, that it correlates with the size of chromatin-associated complexes, but

368 can be locally undermined by active replication or stabilised in non-replicating senescent
369 cells. Importantly, we demonstrate for the first time that nanoscale zonation occurs in both
370 eu- and heterochromatic (A/B) compartments of the nucleus, deviating from previous models
371 of wholly active 'open' vs inactive 'closed' domains. We postulate that genome segments
372 with fewer active sites form larger, low-surface, globular blobs (~1 Mb, ~5000 nucleosomes,
373 ~300-500 nm diameter), while segments rich in active sites display an extended, high-
374 surface, topology of smaller volumes (size range ~0.2 Mb, ~1000 nucleosomes, 150-200 nm
375 diameter). In this model the ratio of active surface area to volume is a key determinant of
376 genome activity (Fig. 6b), while providing an explanation of how cell type specific
377 transcriptional programs can be established despite variation in the genomic composition of
378 A/B compartments between cells[48].
379 Finally, we show cohesin activity to be dispensable for maintaining an interphase
380 filament of consecutive blobs (Fig. 6c, right), in line with a recent study[17]. Given that cohesin
381 is essential for TADs in Hi-C we conclude that chromatin blobs are distinct and not
382 analogous to TADs (Fig. 6c, left). This is consistent with the loop extrusion hypothesis that
383 proposes that TADs emerge in Hi-C experiments due to averaging intermediates of loop
384 extrusion from many cells. The work presented provides a universal structural and dynamic
385 framework of 4D nucleome organisation that guides/modulates the probability of protein
386 (complex)-DNA interactions, thereby changing our perspective of the 3D context in which we
387 frame our knowledge of molecular mechanisms regulating genome function (for further
388 details see Supplementary Discussion).
389
390 **Acknowledgements**
391 We thank Edith Heard for providing FISH probes against X-chromosomal TADs. Imaging
392 was performed at the Micron Oxford Advanced Bioimaging Unit funded by a Wellcome Trust
393 Strategic Award (091911 and 107457/Z/15/Z). L.S. further acknowledges support by the
394 John Fell Oxford University Press (OUP) Research Fund 143/064 and by the European
395 Union's Horizon 2020 research and innovation program under the Marie Sklodowska-Curie
396 Grant Agreement No. 766181. A research visit of H.A.S. in the L.S. lab was enabled by an
397 AfOx travel grant of the Africa-Oxford Initiative. E.M. further acknowledges support by the
398 Sydney Perry Foundation & Covenantors Educational Fund. S.d.O. was supported by grants
399 from the BBSRC (BB/L01811X/1) and the MRC (MR/N00969X/1). V.B. and J.B.
400 acknowledge funding by the MRC (MC_UU_12009). We thank all colleagues who read and
401 provided comments on the manuscript, in particular Jiri & Claudia Lukas, Tim Nott and Rob
402 Klose for valuable suggestions.

Author Contributions

E.M. and L.S. conceived the project and designed the experiments. E.M., R.O., H.A.S. and D.M.S.P. wrote the software and performed analyses. J.B. and V.B. devised the FISH protocol. E.M., R.O., J.B., A.R.C.F., S.d.O., C.I., J.R. and L.S. carried out experiments. E.M., R.O. and L.S. wrote the manuscript and generated the figures with contributions from all authors.

411 **REFERENCES**

412 1. Gibcus, J. H. & Dekker, J. The Hierarchy of the 3D Genome. *Mol. Cell* **49,** 773–782 (2013).
413 2. Pombo, A. & Dillon, N. Three-dimensional genome architecture: players and mechanisms. *Nat.*
414 *Rev. Mol. Cell Biol.* **16,** 245–257 (2015).
415 3. Luger, K., Mäder, A. W., Richmond, R. K., Sargent, D. F. & Richmond, T. J. Crystal structure
416 of the nucleosome core particle at 2.8 A resolution. *Nature* **389,** 251–60 (1997).
417 4. Cremer, T. & Cremer, C. Chromosome territories, nuclear architecture and gene regulation in
418 mammalian cells. *Nat. Rev. Genet.* **2,** 292–301 (2001).
419 5. Adriaens, C. *et al.* Blank spots on the map: some current questions on nuclear organization
420 and genome architecture. *Histochem. Cell Biol.* **150,** 579–592 (2018).
421 6. Lieberman-Aiden, E. *et al.* Comprehensive Mapping of Long-Range Interactions Reveals
422 Folding Principles of the Human Genome. *Science.* **326,** 289–293 (2009).
423 7. Dixon, J. R. *et al.* Topological domains in mammalian genomes identified by analysis of
424 chromatin interactions. *Nature* **485,** 376–380 (2012).
425 8. Lupiáñez, D. G. *et al.* Disruptions of topological chromatin domains cause pathogenic rewiring
426 of gene-enhancer interactions. *Cell* **161,** 1012–1025 (2015).
427 9. Phillips, J. E. & Corces, V. G. CTCF: Master Weaver of the Genome. *Cell* **137,** 1194–1211
428 (2009).
429 10. Parelho, V. *et al.* Cohesins Functionally Associate with CTCF on Mammalian Chromosome
430 Arms. *Cell* **132,** 422–433 (2008).
431 11. Alipour, E. & Marko, J. F. Self-organization of domain structures by DNA-loop-extruding
432 enzymes. *Nucleic Acids Res.* **40,** 11202–11212 (2012).
433 12. Fudenberg, G. *et al.* Formation of Chromosomal Domains by Loop Extrusion. *Cell Rep.* **15,**
434 2038–2049 (2016).
435 13. Ganji, M. *et al.* Supplementary materials for Real-time imaging of DNA loop extrusion by
436 condensin. *Science.* **360,** 102–105 (2018).
437 14. Rao, S. S. P. *et al.* Cohesin Loss Eliminates All Loop Domains. *Cell* **171,** 305–320.e24 (2017).
438 15. Nagano, T. *et al.* Single-cell Hi-C reveals cell-to-cell variability in chromosome structure.
439 *Nature* **502,** 59–64 (2013).
440 16. Flyamer, I. M. *et al.* Single-nucleus Hi-C reveals unique chromatin reorganization at oocyte-to-
441 zygote transition. *Nature* **544,** 110–114 (2017).
442 17. Bintu, B. *et al.* Super-resolution chromatin tracing reveals domains and cooperative
443 interactions in single cells. *Science.* **362,** eaau1783 (2018).
444 18. Finn, E. H. *et al.* Heterogeneity and Intrinsic Variation in Spatial Genome Organization. *Cell*
445 (2019). doi:10.1016/j.cell.2019.01.020
446 19. Nora, E. P. *et al.* Spatial partitioning of the regulatory landscape of the X-inactivation centre.
447 *Nature* **485,** 381–385 (2012).
448 20. Fabre, P. J. *et al.* Nanoscale spatial organization of the *HoxD* gene cluster in distinct

449 transcriptional states. *Proc. Natl. Acad. Sci.* **112,** 13964–13969 (2015).
450 21. Szabo, Q. *et al.* TADs are 3D structural units of higher-order chromosome organization in
451 Drosophila. *Sci. Adv.* **4,** 1–14 (2018).
452 22. Maeshima, K. *et al.* Nucleosomal arrays self-assemble into supramolecular globular structures
453 lacking 30-nm fibers. *EMBO J.* **35,** 1115–1132 (2016).
454 23. Boettiger, A. N. *et al.* Super-resolution imaging reveals distinct chromatin folding for different
455 epigenetic states. *Nature* **529,** 418–422 (2016).
456 24. Maeshima, K. *et al.* The physical size of transcription factors is key to transcriptional regulation
457 in chromatin domains. *J. Phys. Condens. Matter* **27,** 064116 (2015).
458 25. Schermelleh, L. *et al.* Super-resolution microscopy demystified. *Nat. Cell Biol.* **21,** 72–84
459 (2019).
460 26. Schermelleh, L. *et al.* Subdiffraction Multicolor Imaging of the Nuclear Periphery with 3D
461 Structured Illumination Microscopy. *Science.* **320,** 1332–1336 (2008).
462 27. Markaki, Y. *et al.* Functional nuclear organization of transcription and DNA replication: A
463 topographical marriage between chromatin domains and the interchromatin compartment.
464 *Cold Spring Harb. Symp. Quant. Biol.* **75,** 475–492 (2010).
465 28. Smeets, D. *et al.* Three-dimensional super-resolution microscopy of the inactive X
466 chromosome territory reveals a collapse of its active nuclear compartment harboring distinct
467 Xist RNA foci. *Epigenetics Chromatin* **7,** 8 (2014).
468 29. Kanda, T., Sullivan, K. F. & Wahl, G. M. Histone–GFP fusion protein enables sensitive
469 analysis of chromosome dynamics in living mammalian cells. *Curr. Biol.* **8,** 377–385 (1998).
470 30. Jao, C. Y. & Salic, A. Exploring RNA transcription and turnover in vivo by using click chemistry.
471 *Proc. Natl. Acad. Sci.* **105,** 15779–15784 (2008).
472 31. Shaban, H. A., Barth, R. & Bystricky, K. Formation of correlated chromatin domains at
473 nanoscale dynamic resolution during transcription. *Nucleic Acids Res.* **46,** e77 (2018).
474 32. Bruinsma, R., Grosberg, A. Y., Rabin, Y. & Zidovska, A. Chromatin hydrodynamics. *Biophys.*
475 *J.* **106,** 1871-1881 (2014).
476 33. Markaki, Y. *et al.* The potential of 3D-FISH and super-resolution structured illumination
477 microscopy for studies of 3D nuclear architecture. *BioEssays* **34,** 412–426 (2012).
478 34. Brown, J. M. *et al.* A tissue-specific self-interacting chromatin domain forms independently of
479 enhancer-promoter interactions. *Nat. Commun.* **9,** 1–15 (2018).
480 35. Zuin, J. *et al.* Cohesin and CTCF differentially affect chromatin architecture and gene
481 expression in human cells. *Proc. Natl. Acad. Sci.* **111,** 996–1001 (2014).
482 36. Kraus, F. *et al.* Quantitative 3D structured illumination microscopy of nuclear structures. *Nat.*
483 *Protoc.* **12,** 1011-1028 (2017).
484 37. Fakan, S. & van Driel, R. The perichromatin region: A functional compartment in the nucleus
485 that determines large-scale chromatin folding. *Semin. Cell Dev. Biol.* **18,** 676–681 (2007).
486 38. Nozawa, R. S. *et al.* SAF-A Regulates Interphase Chromosome Structure through
487 Oligomerization with Chromatin-Associated RNAs. *Cell* **169,** 1214–1227.e18 (2017).

488 39. Zhao, R., Nakamura, T., Fu, Y., Lazar, Z. & Spector, D. L. Gene bookmarking accelerates the
489 kinetics of post-mitotic transcriptional re-activation. *Nat. Cell Biol.* **13,** 1295–1304 (2011).
490 40. Dambacher, S., Hahn, M. & Schotta, G. Epigenetic regulation of development by histone lysine
491 methylation. *Heredity (Edinb).* **105,** 24–37 (2010).
492 41. Schotta, G. *et al.* A silencing pathway to induce H3-K9 and H4-K20 trimethylation at
493 constitutive heterochromatin. *Genes Dev.* **18,** 1251-1262 (2004).
494 42. Rowley, M. J. & Corces, V. G. Organizational principles of 3D genome architecture. *Nat. Rev.*
495 *Genet.* **13,** (2018).
496 43. Chagin, V. O. *et al.* 4D Visualization of replication foci in mammalian cells corresponding to
497 individual replicons. *Nat. Commun.* **7,** 11231 (2016).
498 44. Albiez, H. *et al.* Chromatin domains and the interchromatin compartment form structurally
499 defined and functionally interacting nuclear networks. *Chromosom. Res.* **14,** 707–733 (2006).
500 45. Gorisch, S. M. *et al.* Nuclear body movement is determined by chromatin accessibility and
501 dynamics. *Proc. Natl. Acad. Sci.* **101,** 13221-13226 (2004).
502 46. Maeshima, K., Hihara, S. & Eltsov, M. Chromatin structure: Does the 30-nm fibre exist in vivo?
503 *Curr. Opin. Cell Biol.* **22,** 291–297 (2010).
504 47. Natsume, T., Kiyomitsu, T., Saga, Y. & Kanemaki, M. T. Rapid Protein Depletion in Human
505 Cells by Auxin-Inducible Degron Tagging with Short Homology Donors. *Cell Rep.* **15**, 210-218
506 (2016).
507 48. Joffe, B., Leonhardt, H. & Solovei, I. Differentiation and large scale spatial organization of the
508 genome. *Curr. Opin. Genet. Dev.* **20,** 562–569 (2010).
509

510 **FIGURES**

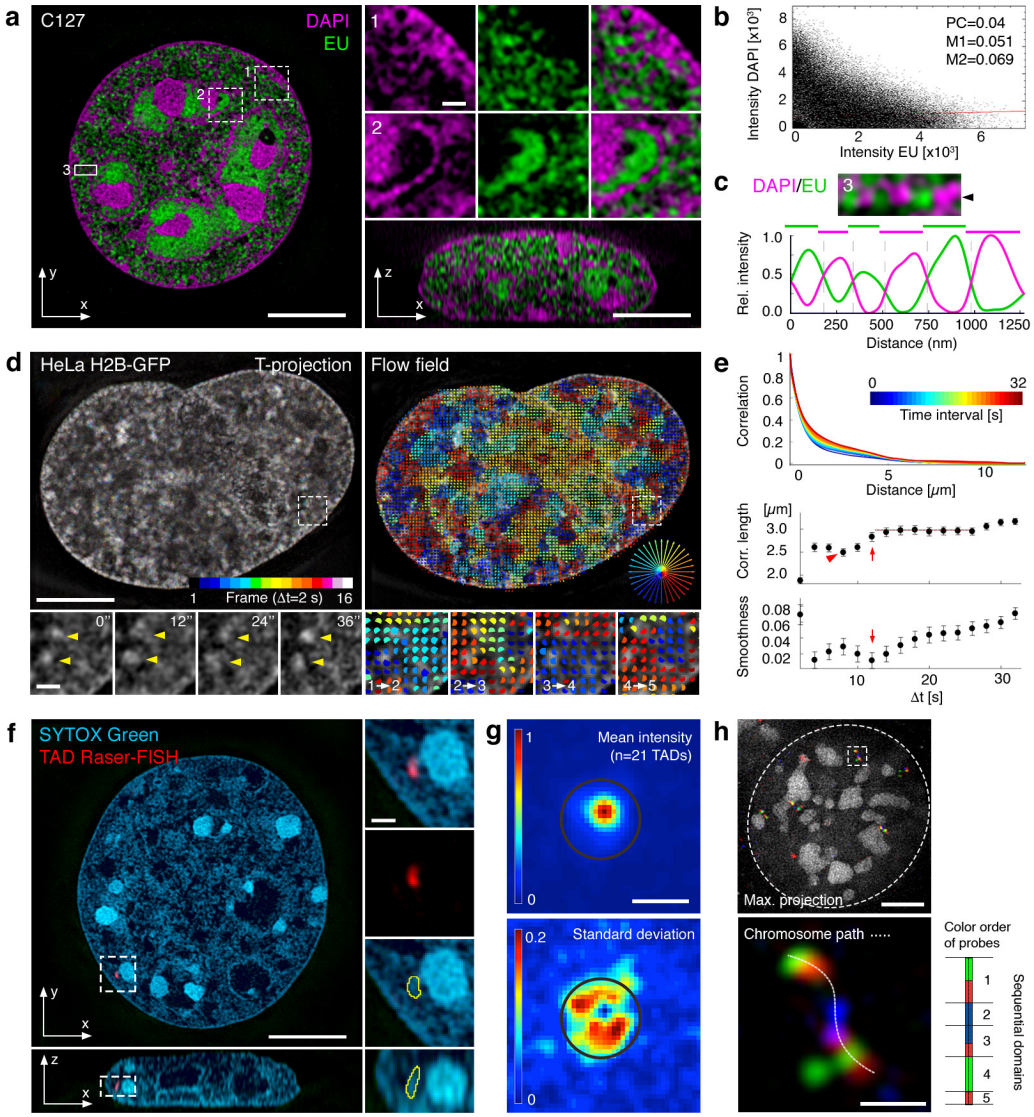

511
512

513 **Figure 1 | Chromatin folds into a 3D filament of 'blobs' distinct from an RNA-occupied**
514 **interchromatin network. a**, Super-resolution 3D-SIM of fixed mouse C127 mammary
515 epithelial cells resolves DAPI-stained chromatin as a porous convoluted filament juxtaposed
516 to a volume of non-chromatin (interchromatin, IC) channels where RNA resides (EU, 60 min
517 pulse). Right, inset magnifications of regions 1 and 2, and orthogonal cross section. **b**, Pixel-
518 based colocalisation analysis scatter plot confirms anti-correlation of DAPI and EU signal.
519 PC: Pearson correlation coefficient; M1/M2: Manders' correlation coefficients DAPI vs. EU
520 and EU vs. DAPI, respectively. **c**, Line profile of signal intensity for both DAPI and EU from a
521 representative euchromatic region in panel (a) reveal mutually exclusive volumes occupied
522 by both nucleic acids. **d,** Live cell 3D-SIM of a human HeLa cell stably expressing histone
523 H2B-GFP. Left panel: Colour-coded projection of 16 consecutive time-points recorded with
524 2 s intervals (Supplementary Movie 1). Inset magnifications of selected individual time-points
525 showing coherently moving domains (arrow heads). Right panel: Overlay of flow field
526 indicating motion direction. Fields are colour-coded according to the direction of the
527 displacement (Supplementary Movie 4). Insets show analyses for the first 4 intervals with a

time lag of 1 frame (Δ=2 s). **e**, Correlation function (top) is calculated as a function of distance at every accessible time interval (Δt colour coded from short to high time intervals, from blue to red, respectively) within the image series and each of them was fitted to the Whittle–Matérn model. Correlation length (middle) and smoothness parameter (bottom) are calculated over time for directional correlation of flow fields. Further quantitative analysis of motion fields was performed to extract biophysical parameters and types of motions to characterize diffusion processes at different scales (Methods; Extended Data Fig. 2b). **f**, RASER-FISH detection of a 0.7 Mb labelled TAD (red) and SYTOX Green whole chromatin labelling (cyan) in a mouse C127 cell imaged by 3D-SIM. **g**, Quantification of the mean intensity of 21 TADs. For each TAD, the z-plane containing the brightest pixel was selected, centred with respect to this pixel and normalized to its signal intensity (top). The standard deviation (SD, bottom) describes the degree of variation in TAD size, indicated with a diameter of ~500 nm. **h**, Multicolour FISH labelling of sequential domains across the α-globin gene locus detected in mouse C127 cells. Maximum projections of 3D-SIM micrographs show the genomic order of the probes is preserved as a curvilinear filament of discrete chromatin blobs in space. Scale bars: 5 μm and 0.5 μm (insets).

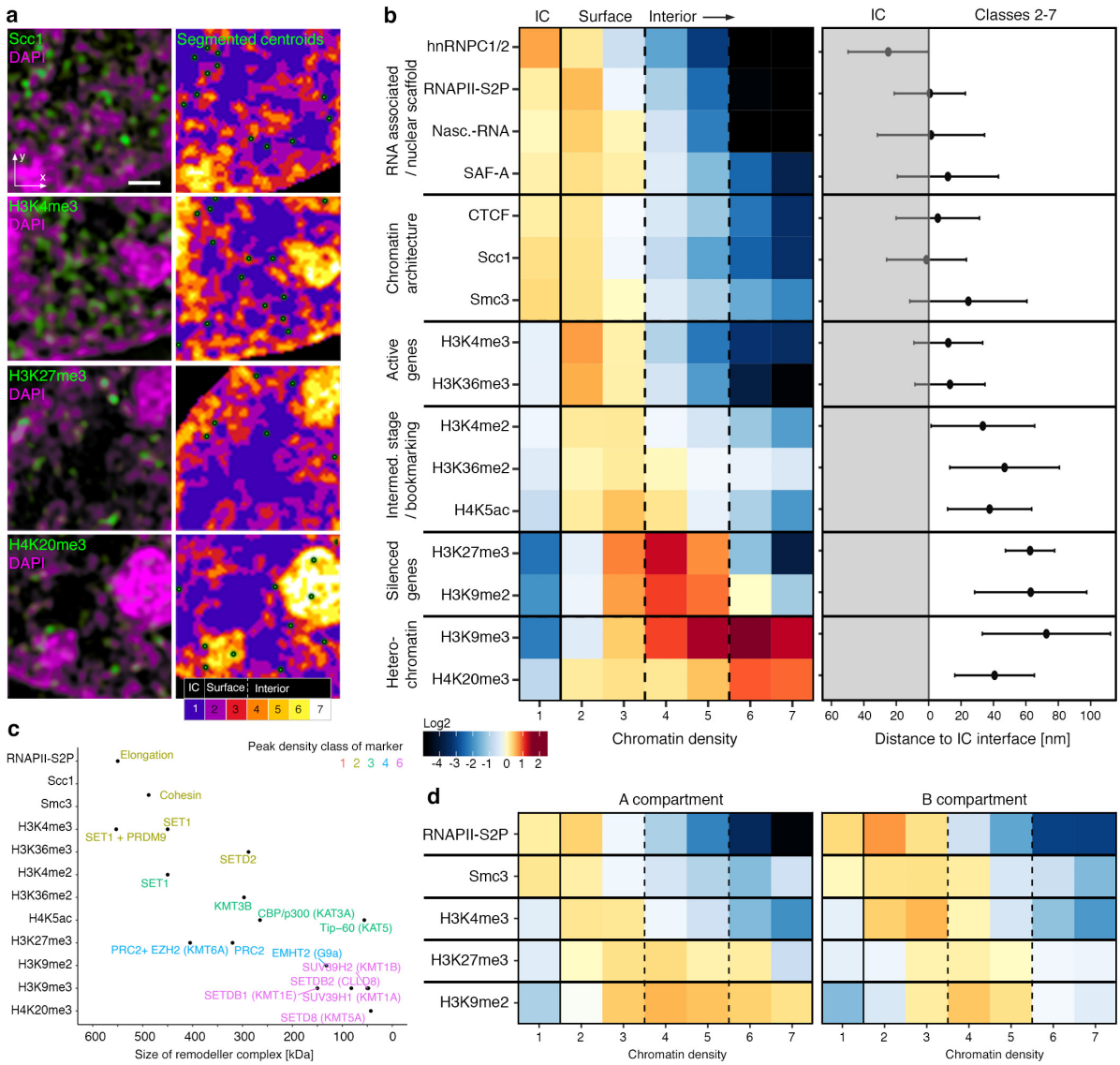

Figure 2 | Functional marker distribution in somatic cells reveals nanoscale 3D zonation correlated with protein complex size. a, Representative single Z planes of 3D-SIM image stacks comparing the spatial localization of different markers with respect to chromatin. Marker centroid coordinates are depicted as green dots with a black outline for regions where the centroid is in the z plane shown. Scale bar: 0.5 μm. **b**, Left: Heatmap of enrichment or depletion of IF signals relative to a random distribution (plotted in log2-fold change) per chromatin density class for all markers. Right: Distance to the chromatin-IC boundary for all markers. Distances on the left (grey) emanate from the IC and on the right (white) emanate from chromatin. The mean distance and 95% confidence interval of the population are shown. N = 433 cells. **c**, Scatterplot showing the correlation between the size of the chromatin complexes corresponding to each of the analysed markers and the peak chromatin class where each marker is found. MW for cohesin was calculated from Smc1, Smc3, Scc1 and Scc3. **d**, Heatmaps relative IF signals distribution of representative markers in nuclear sub-volumes harbouring mainly heterochromatin characteristic for B compartments (segmented perinuclear rim and chromocenter regions), or euchromatin characteristic for A compartments (remaining volume). Both compartments show a relatively

conserved zonation pattern despite the different composition of chromatin density in either A or B regions (Extended Data Fig. 5d). N = 170 cells.

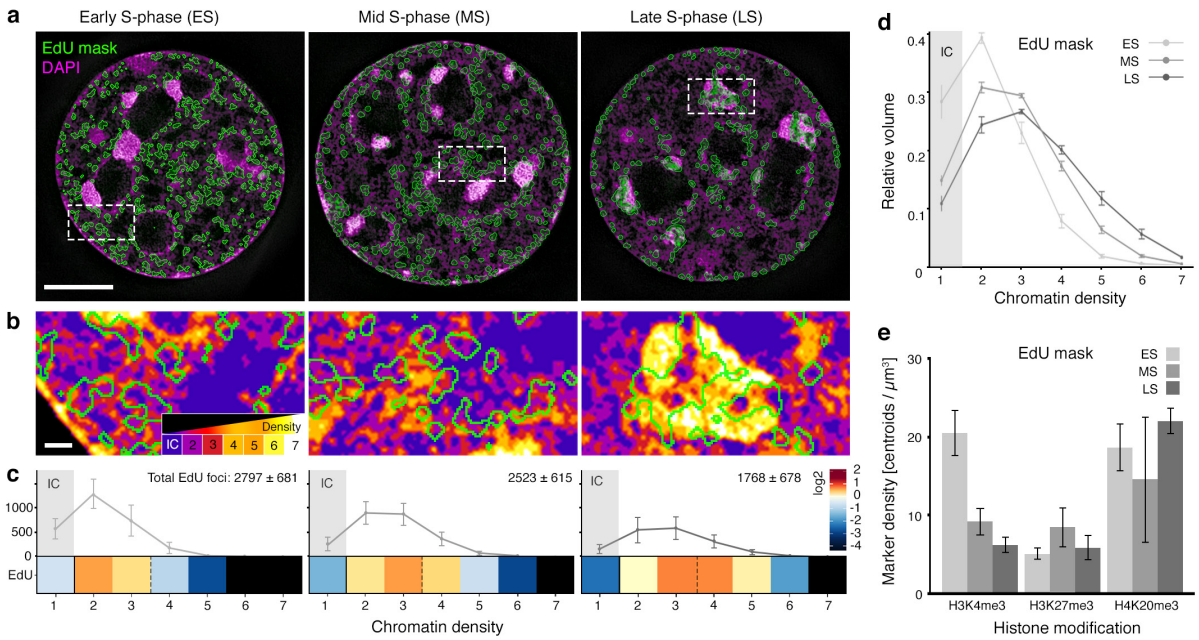

Figure 3 | Effect of active replication and replicative senescence on chromatin composition. a, Representative single Z planes of 3D-SIM images showing the chromatin landscape with the different patterns of replication (green) during S-phase progression from early, mid and late S-phase stages (left to right). Chromatin is stained with DAPI and replication is stained using 15 minutes of EdU incorporation. Local replication regions were masked based on the EdU signal and outlined in green. Scale bar: 5 μm. **b**, Insets of respective boxes indicated in A in which the EdU submask (green outline) is overlaid on the segmented chromatin landscape. Scale bar: 0.5 μm. **c**, Quantification of the absolute number of detected EdU foci in each of the different chromatin classes. The total number of EdU foci per cell is indicated as mean ± SD. Per S-phase stage, a heatmap of enrichment or depletion of EdU signals relative to a random distribution (plotted in log2-fold change) is depicted. **d**, Percentage of chromatin volume of the different density classes to EdU submask volume per S-phase stage. The mean percentage ± SD are depicted. **e**, Foci number per cubic μm EdU submask volume for the depicted histone PTMs in each condition (Extended Data Fig. 7) per S-phase stage. Mean ± SD are depicted. Number of cells: ES = 225, MS =227, LS =230.

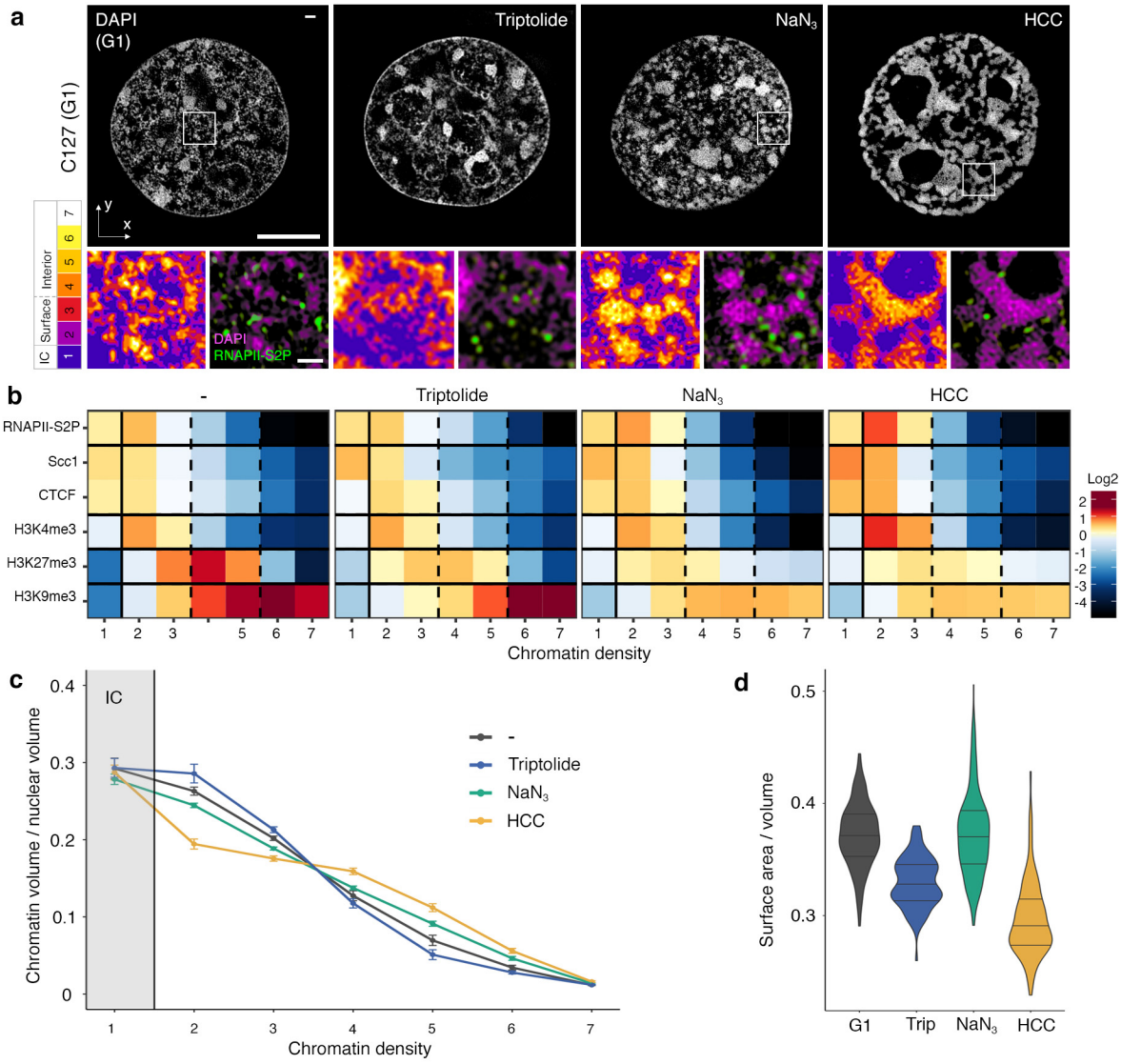

Figure 4 | Epigenome zonation persists after induced perturbation of filament topology. a, Gallery depicting the progressive spatial rearrangement of the filament by the effects of triptolide, sodium azide (NaN_3), hyperosmolarity-induced chromatin compaction (HCC), compared to untreated C127 G1 cells (-). Left insets show density class distribution, right inset shows position of RNAP-S2P at the filament's 3D boundary. **b**, Heatmap of enrichment or depletion of IF signals from a representative subset of markers comparing untreated vs. NaN_3, hyperosmolarity and triptolide treated cells. **c**, Proportion of nuclear volume for each chromatin density class. None of the treatments perturb the IC volume (± 95%CI), but for NaN_3 and HCC there is loss of low-density chromatin (class 2-3) and increase in higher density chromatin (classes 4-7), while triptolide has the opposite effect. **d** Violin plot of surface area to volume ratio of the filament in untreated (-) G1 cells or after treatment with triptolide (Trip), NaN_3or HCC, showing a decrease in filament complexity, quartiles marked. Number of cells: G1 = 210, NaN_3 = 120, HCC =120, Trip=123. Scale bars: 5 μm and 0.5 μm (insets).

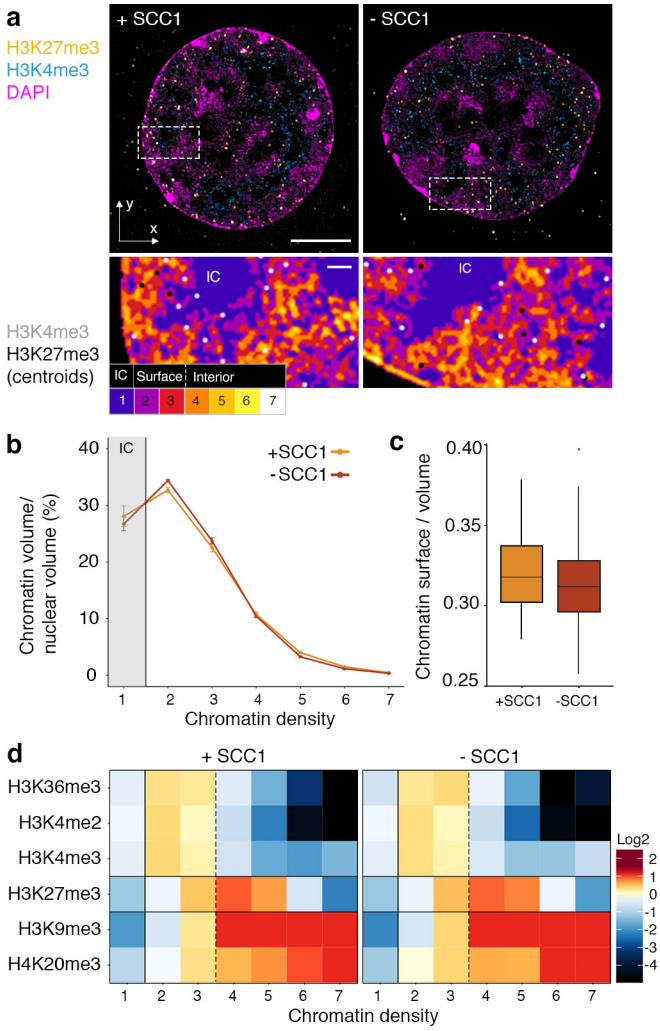

Figure 5 | Cohesin ablation does not affect epigenome topology. a, Representative single z-planes of 3D-SIM images comparing the chromatin landscape in HCT116 cells control cells only treated with auxin for 6 h (+SCC1, left) or SCC1 ablated cells after 16 h doxycycline and 6 h auxin treatment (-SCC1, right). Insets show the segmented landscape with the spatial distribution of H3K4me3 and H3K27me3 represented as green and red dots respectively. **b**, Proportion of nuclear volume for each chromatin density class show no significant change under ablation of cohesin function (± 95%CI). **c**, Heatmap of enrichment or depletion of IF signals from a representative subset of histone modifications. Number of cells: +SCC1 = 80; -SCC1 = 104. Scale bars: 5 μm and 0.5 μm (insets).

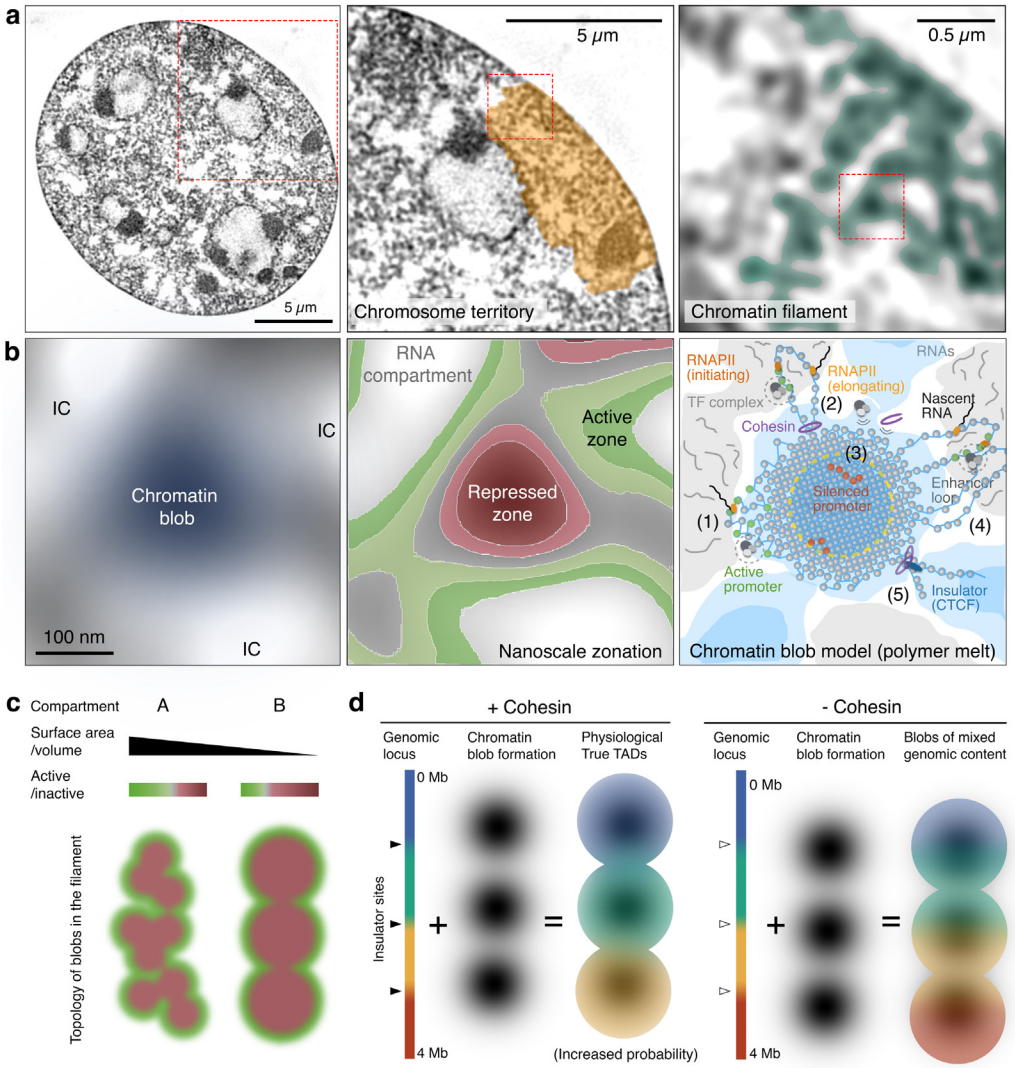

Figure 6 | Model of the chromatin as a filament of blobs. a. Serial magnifications of super-resolved interphase chromatin stained with DAPI in C127 with an overlaid representation of a putative chromosome territory (centre). Chromatin can be described as a curvilinear filament of chromatin blobs. **b**, Zoom-in to an individual blob (left) where zonation at the nm scale is a function of density (centre) modelled by the radial position of histones with diverse PTMs and protein complexes (right). Beyond ~100nm from the blob surface to the IC almost no markers are detected such that any silenced promoter at this "depth" (yellow dashed circle) may remain inactive by being inaccessible to the transcription machinery rather than through competition by deposition of repressive histone PTMs. **c**, The ratio of active surface area to volume is a key determinant of genome activity. Changes in TAD topology in either A or B compartments lead to changes in this ratio and give rise to a generally active vs inactive compartment. **d**, Folding of the genome into biophysically defined blobs in the absence of cohesin leads to blob structures without physiologically relevance (multiple colours mixed over genomic insulator boundaries, right). Addition of cohesin, while dispensable for globule formation, links the 3D structure to the correct 1D genomic context leading to physiologically relevant interactions observed as "true TADs" in population Hi-C (left)**.**

632 **EXTENDED DATA FIGURES**

633

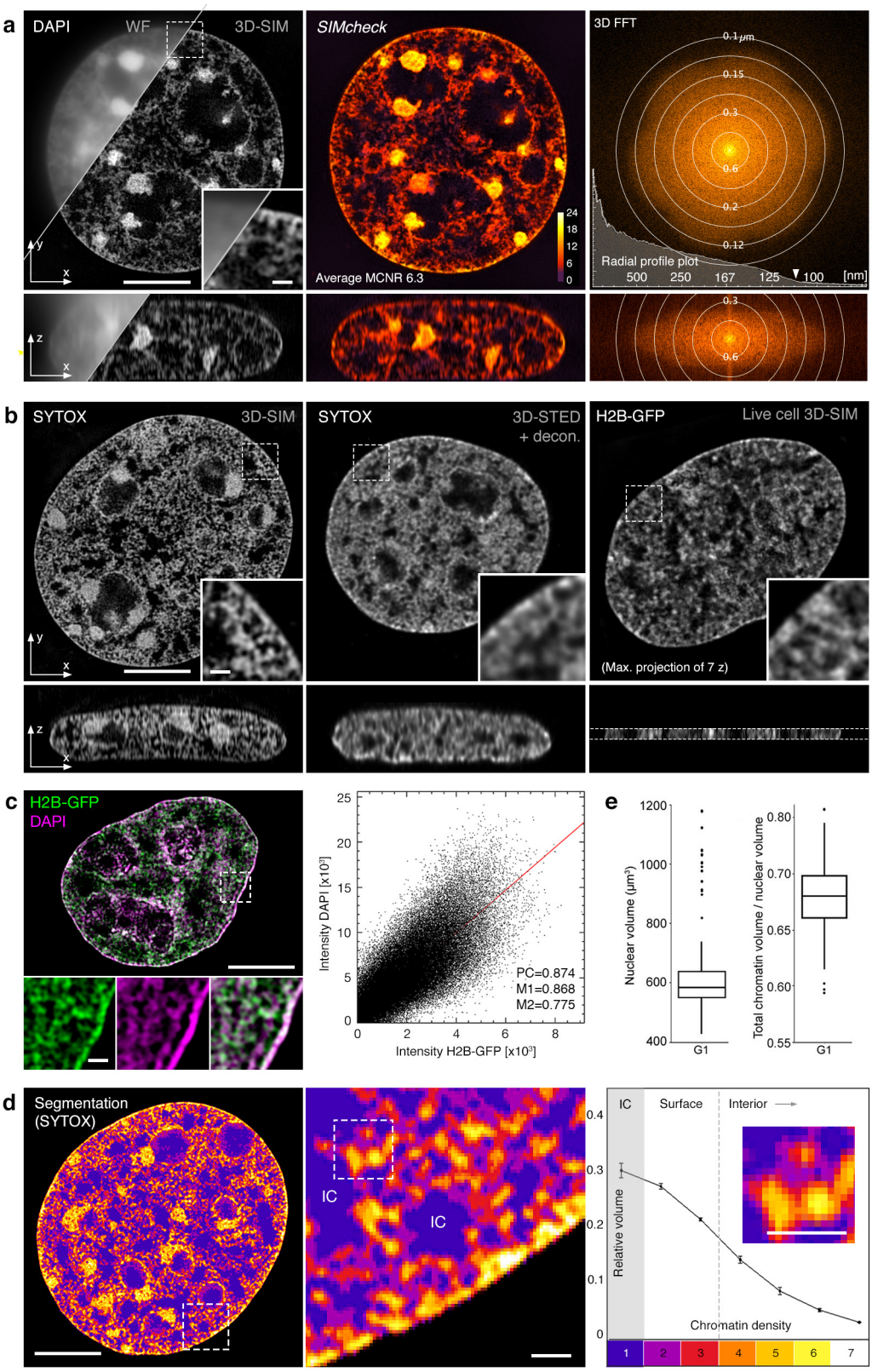

634

635

636 **Extended Data Figure 1 | Super-resolution imaging of chromatin. a**, 3D-SIM data quality
637 control. Left panel: Comparison of widefield (WF) and corresponding 3D-SIM image of a
638 mouse C127 cell nucleus stained with DAPI (excited with 405 nm, detected in green

639 emission of 500-550 nm); lateral (top) and orthogonal (bottom) cross section is displayed.
640 Middle and right panel: corresponding quality control analysis using SIMcheck[53], showing a
641 mapping of local stripe modulation contrast (MCNR, modulation contrast to noise ratio) on
642 the reconstructed cross section (middle), and the corresponding axial and lateral Fourier plot
643 with corresponding spatial resolution indicated by concentric rings (right). Superimposed
644 radial profile plot indicates an effective lateral resolution of ~110 nm (arrow head). **b**,
645 Comparison of 3D-SIM (left) and 3D STED (middle) of formaldehyde fixed cells stained with
646 DAPI or SYTOX green staining in C127 cells, as well as live cell 3D-SIM of histone H2B-
647 GFP in a human RPE-1 epithelial cell (right, projection of 7 z-planes covering 0.75 μm
648 depth). In all cases, 3D super-resolution imaging allows to resolve filamentous chromatin
649 organisation with globular features and IC network. **c**, DAPI-stained fixed H2B-GFP 3D-SIM
650 and corresponding colocalisation analysis shows strong correlation of both signals. PC:
651 Pearson correlation coefficient; M1/M2: Manders' correlation coefficients DAPI vs. H2B-GFP
652 and H2B-GFP vs. DAPI, respectively. **d**, Segmentation of chromatin staining into 7 intensity
653 (density) classes (Methods) distinguishes interchromatin (IC, class 1) from chromatin of
654 increasing density (classes 2-7). Chromatin density classification serves as a proxy for
655 surface and interior regions of filamentous chromatin. Right: Quantification of class sizes
656 show a decrease of nuclear volume fractions as density increases. **e**, Quantification of
657 nuclear volumes in C127 G1 cells from all segmented voxels shows a mean of ~600 μm^3, of
658 which 68% is occupied by segmented chromatin (classes 2-7). Scale bars: 5 μm and 0.5 μm
659 (insets).

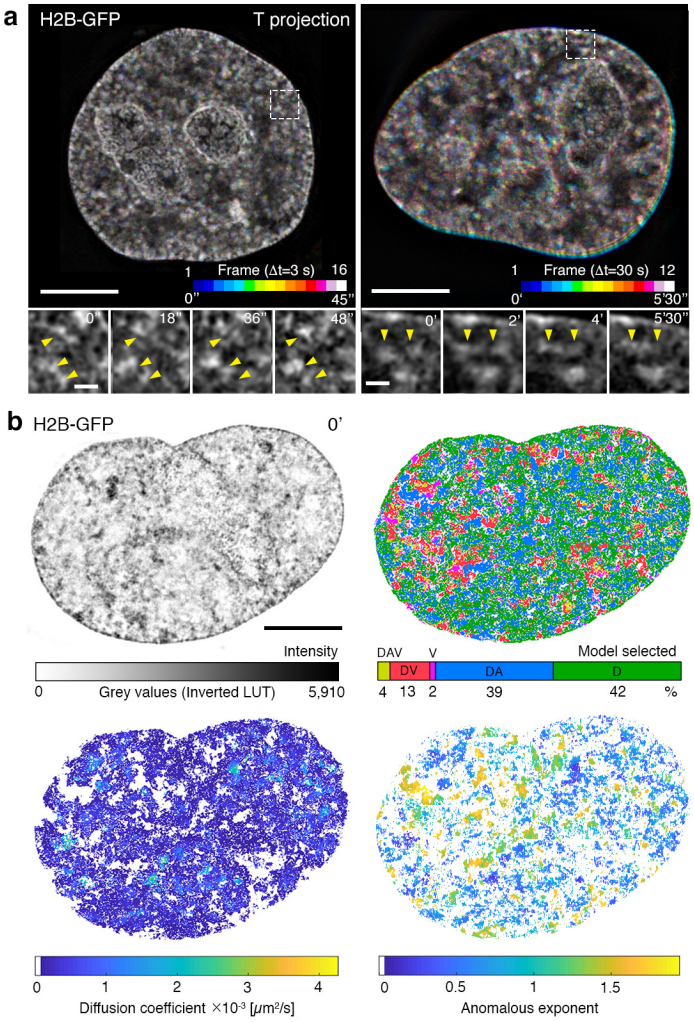

Extended Data Figure 2 | Analysis of chromatin dynamics in from live cell 3D-SIM. a, Live cell 3D-SIM of human HeLa cells stably expressing histone H2B-GFP recorded with intervals of 3 s (left, Supplementary Movie 2) and 30 s (right, Supplementary Movie 3). Colour-coded projection of 16 consecutive time-points. Inset magnifications show selected time-points of the boxed region as maximum projection of 7 z-sections (0.75 μm depth). **b**, Quantitative analysis of motion fields is applied using Bayesian model selection to define types of diffusion processes acting on the chromatin fibre at the local and global scale[49]. The spatial distribution of the selected models for each pixel is shown as a colour map (top right), where D: Free diffusion; DA: Anomalous diffusion; V: Drift velocity of flow fields; DV: Free diffusion + drift; DAV Anomalous diffusion + drift. The mapping of diffusion constants and anomalous coefficient in the lower panels highlight the heterogeneity of chromatin motion. Scale bars: 5 μm and 0.5 μm (insets).

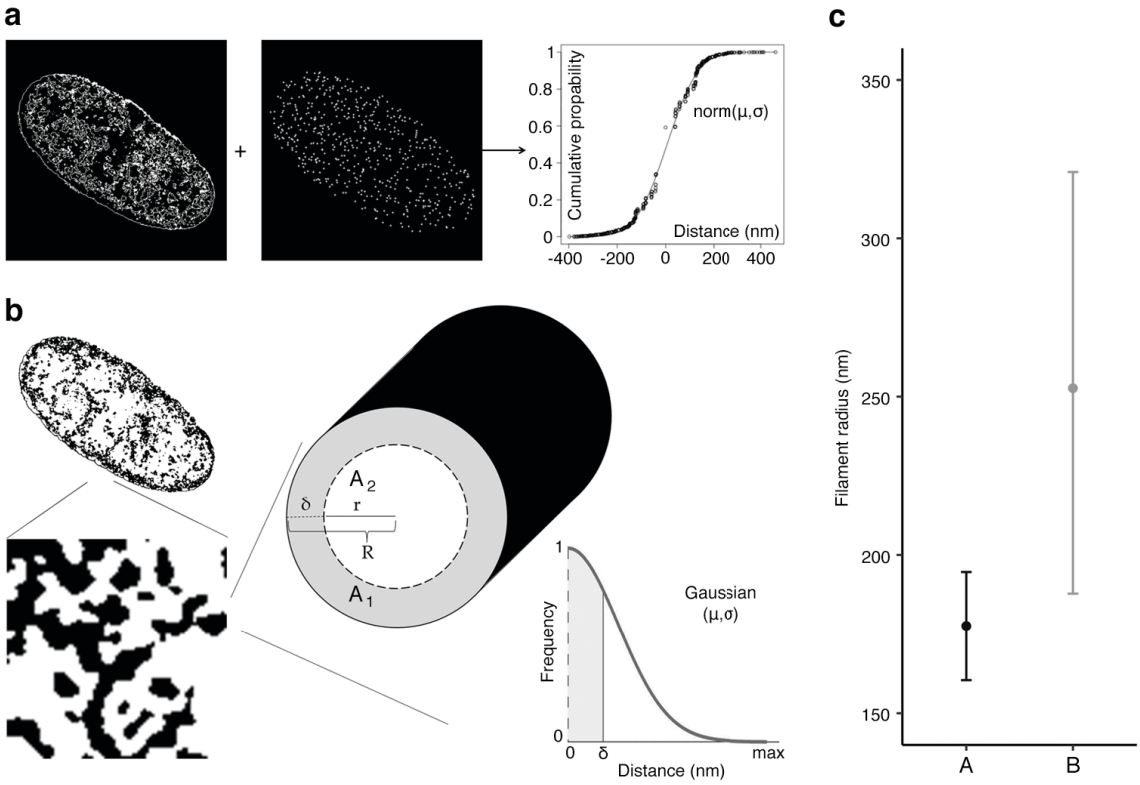

Extended Data Figure 3 | Calculation of filament dimensions. a, A random scatter of 3D points in silico (restrained to the volume of the nucleus, centre) can be used to calculate a random sampling of distances to the boundary (left) between the IC and filament signal. A least square fitting to the cumulative probability of the whole distribution yields mean distance (μ) and standard deviation (σ). **b**, From empirical observation the filament can be approximated as a sponge-like structure of tubular filaments with a degree of variability in width but with an average radius of R. From this model, by simple calculus, the average radius of the filament can be calculated (Methods). **c**, Separating the nuclear volume into macro-scale A and B compartments defined by the lack or presence of lamina-association and chromocenter-morphology yields a filament radius of 175 nm for the more tubular like A compartment (diameter 350 nm). The B compartment is larger, however, being less tube-like there is decrease accuracy in radial estimation (error bars 95% confidence).

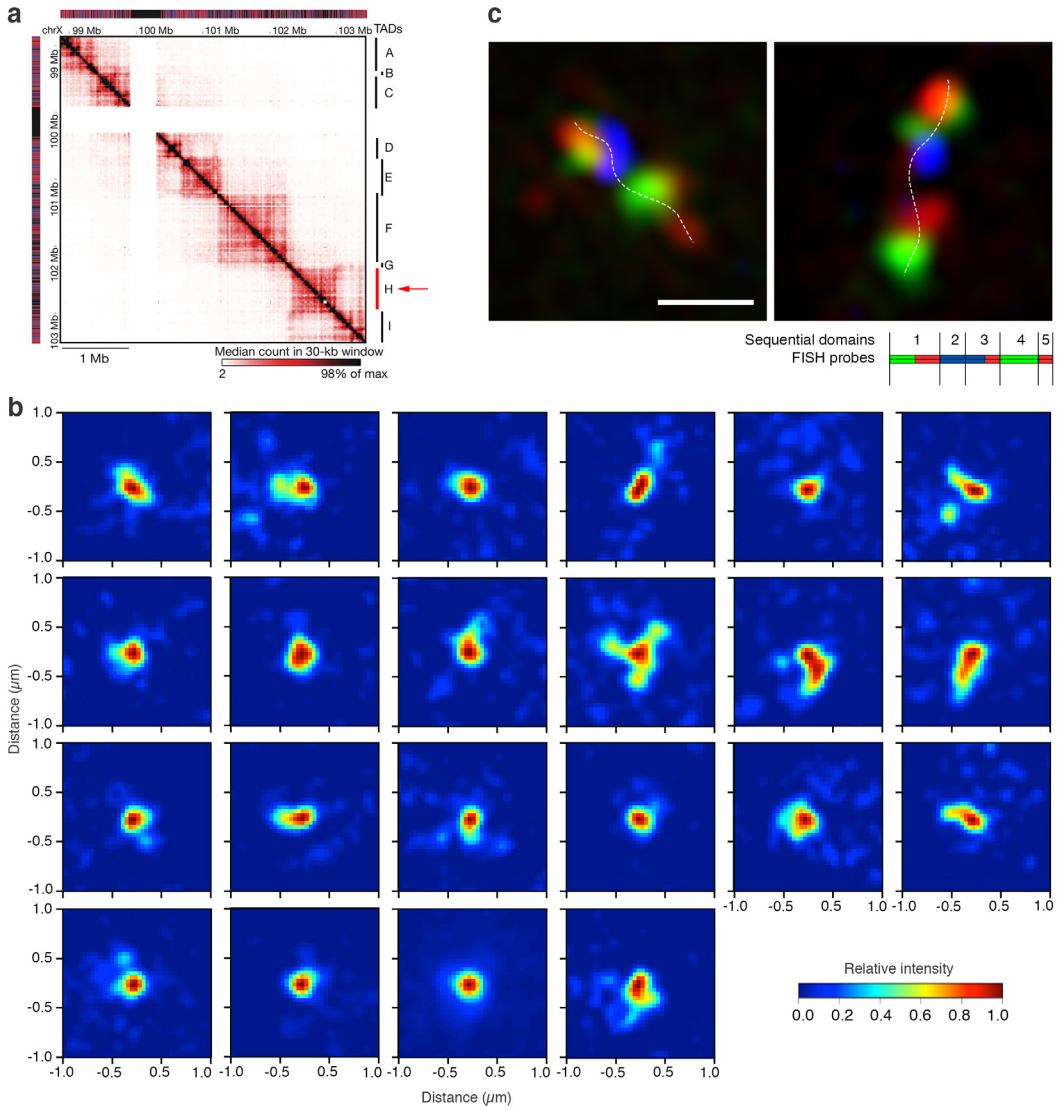

Extended Data Figure 4 | RASER-FISH for imaging chromatin conformation. a, Hi-C heatmap showing the interaction frequency in the 700kb probe (probe H, red bar) used in this study for subsequent RASER-FISH experiments (adapted from[19]). **b**, Super-resolved heatmaps of single Z planes of H TADs on the active X chromosome. TADs were selected based on the absence of the inactive Barr body and for the displayed z planes to contain the brightest pixel of the TAD z-stack. Signal intensity was normalized to the brightest pixel. **c**, Max projections 3D-SIM micrographs of multicolour FISH labelling of sequential domains across the α globin locus. The linear genomic order of the probes (green, red, blue, red, green, red) is preserved as a curvilinear path in 3D (dotted line). Scale bar: 0.5 μm.

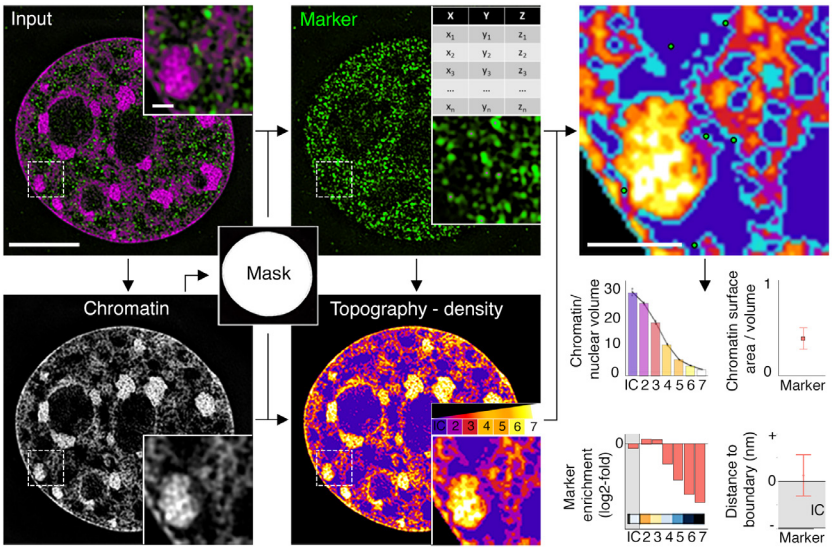

Extended Data Figure 5 | Systematic analysis of the 3D epigenome. Schematic representation of the Cha*i*N analysis workflow. Inputs for the workflow are multi-channel 3D-SIM datasets that have been pre-processed, thresholded and aligned. Firstly, a nucleus mask is generated based on the chromatin channel. Secondly, within this mask, marker spots are segmented by intensity and their weighted centroid positions are determined. Simultaneously, the chromatin channel is segmented in 7 intensity "classes", reflecting increasing chromatin compaction. Finally, metrics from both marker and chromatin channel are used to describe the 3D epigenome, such as the nuclear proportion of each chromatin class, the chromatin surface-to-volume ratio, the marker enrichment or depletion in each chromatin class or the mean distance (± 95% CI) of markers to the segmented chromatin-interchromatin boundary. Analysis was performed using scripts written in R and Octave. Scale bars: 5 μm and 0.5 μm (insets).

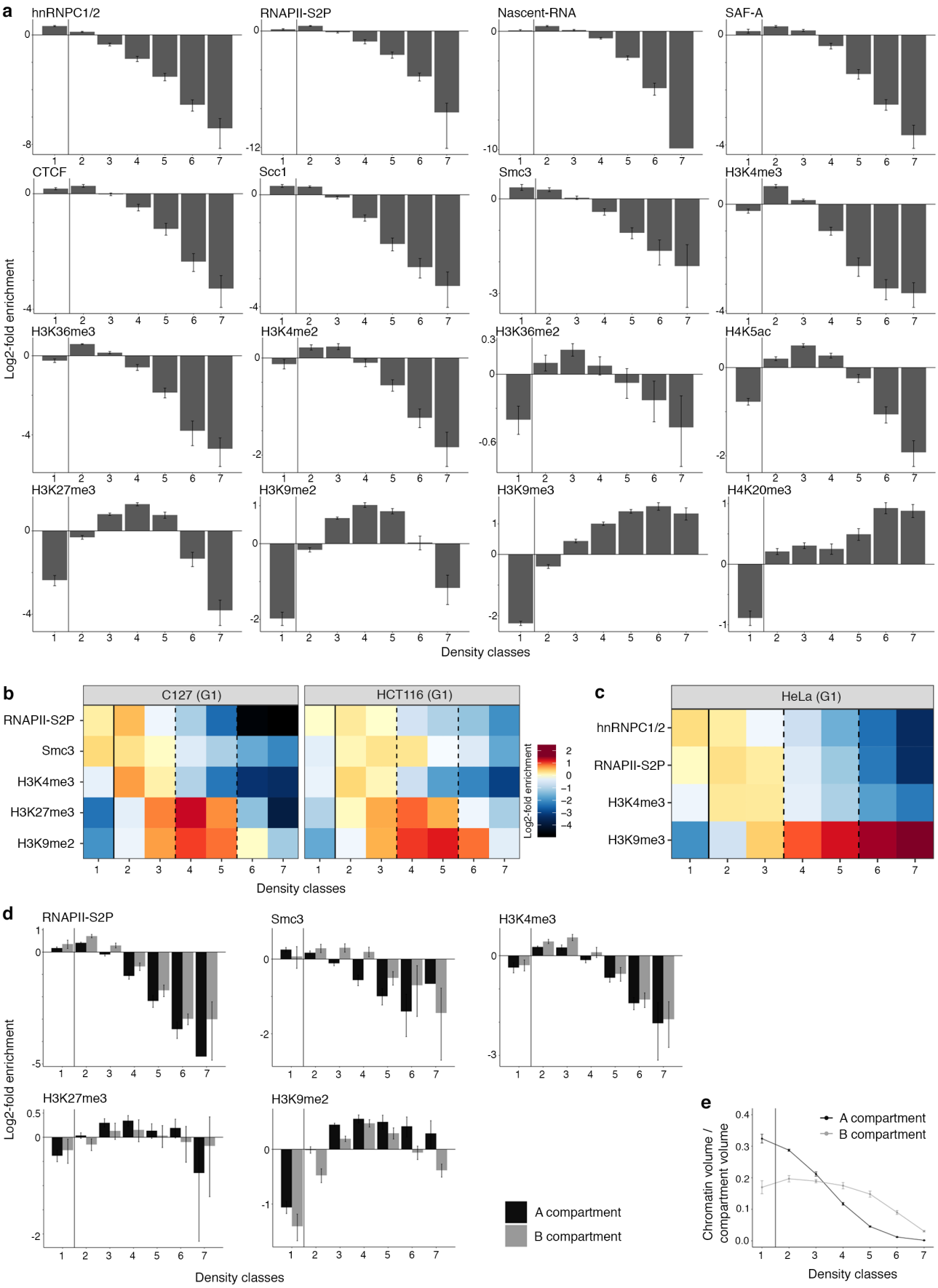
a
hnRNPC1/2
RNAPII-S2P
Nascent-RNA
SAF-A
CTCF
Scc1
Smc3
H3K4me3
H3K36me3
H3K4me2
H3K36me2
H4K5ac
H3K27me3
H3K9me2
H3K9me3
H4K20me3
Log2-fold enrichment
Density classes
b
C127 (G1)
HCT116 (G1)
RNAPII-S2P
Smc3
H3K4me3
H3K27me3
H3K9me2
Log2-fold enrichment
Density classes
c
HeLa (G1)
hnRNPC1/2
RNAPII-S2P
H3K4me3
H3K9me3
d
RNAPII-S2P
Smc3
H3K4me3
H3K27me3
H3K9me2
Log2-fold enrichment
Density classes
A compartment
B compartment
e
Chromatin volume / compartment volume
A compartment
B compartment
Density classes

716

717

718 **Extended Data Figure 6 | Functional marker distribution in whole mouse and human**
719 **cell lines and macro-compartments. a**, Bar plots of the log-2 fold over/under
720 representation of each marker analysed in each of the segmented chromatin classes for G1
721 relative to chromatin class volume. Number of cells = 433. **b**, **c**, Representative selection of
722 markers in mouse C127 mammary epithelial cells show the same zonation pattern with the
723 same antibodies in human HCT116 colon carcinoma cells (b) and HeLa cells (c), suggesting
724 chromatin accessibility as a universal regulator of epigenetic zonation. Number of cells:
725 C127 = 170, HCT116 =70, HeLa = 41. **d**, **e,** Bar plots of the over/under representation of
726 representative marker in each of the segmented G1 macro-scale A/B chromatin
727 compartments showing a relatively conserved zonation pattern between active and
728 repressive markers despite the different composition of chromatin density in either A or B
729 regions (e). Plots show average log-2 value, error bars indicate 95% confidence interval.
730 Number of cells = 170.
731

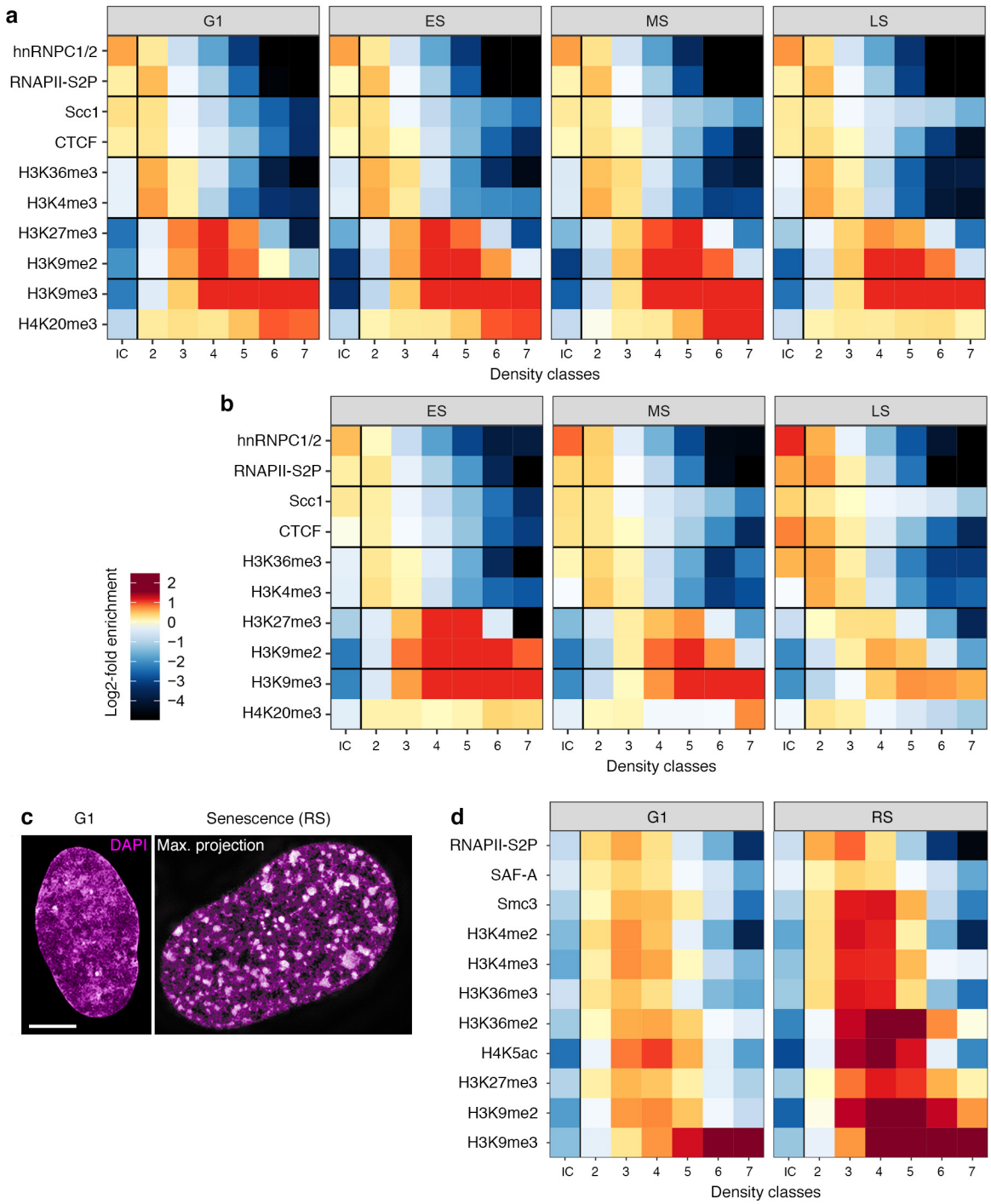

Extended Data Figure 7 | Functional marker distribution in different S-phase stages of mouse C127 mammary epithelial cells and in cycling and senescent human IMR-90 myofibroblast cells. a, Heatmaps of enrichment or depletion of IF signals relative to random (plotted in log2-fold change) per chromatin density class in the whole nuclear volume or EdU-submask (**b**). Number of cells: G1 =320, ES = 225, MS = 227, LS = 230. **c**. Super resolution imaging of DAPI-stained chromatin in G1 or replicative senescent (RS) IMR90 nucleus showing the presence of senescence-associated heterochromatin foci (SAHF). **d**. Heatmaps of enrichment or depletion of IF signals relative to random (plotted in log2-fold change) per chromatin density class in G1 or RS IMR90 cells. G1 = 208 cells, RS = 211 cells.

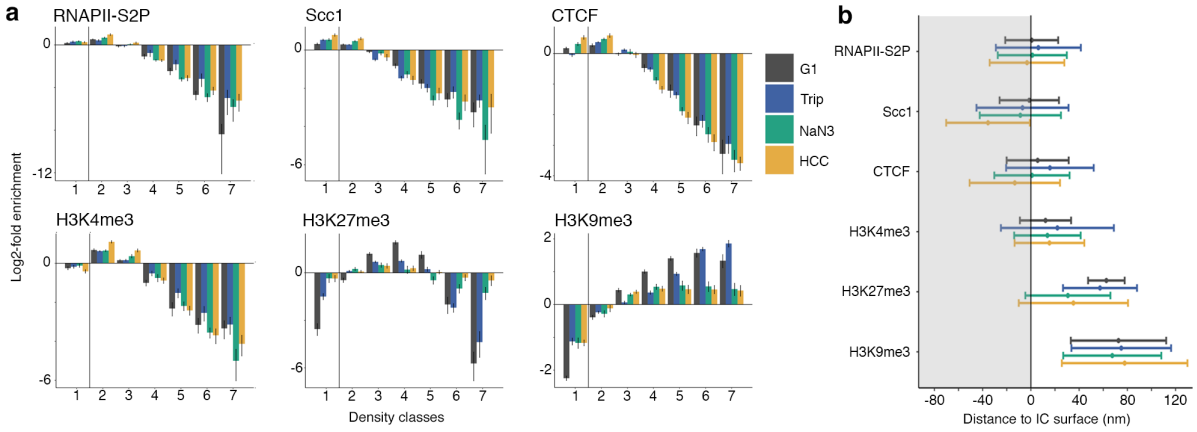

Extended Data Figure 8 | Functional marker distribution upon biophysical or transcriptional perturbation. a, Bar plots of the over/under representation of each histone PTM analysed in each of the segmented chromatin classes for G1, biophysical compaction (NaN_3 or HCC) or transcription initiation inhibition (Trip). Plots show average log-2 value, error bars indicate 95% confidence interval. **b**, Distance (nm) to the chromatin-IC boundary from a representative subset of markers in Figure 2b comparing G1, NaN_3, HCC and Trip. Number of cells: G1 = 210, NaN_3 = 120, HCC =120, Trip=123.

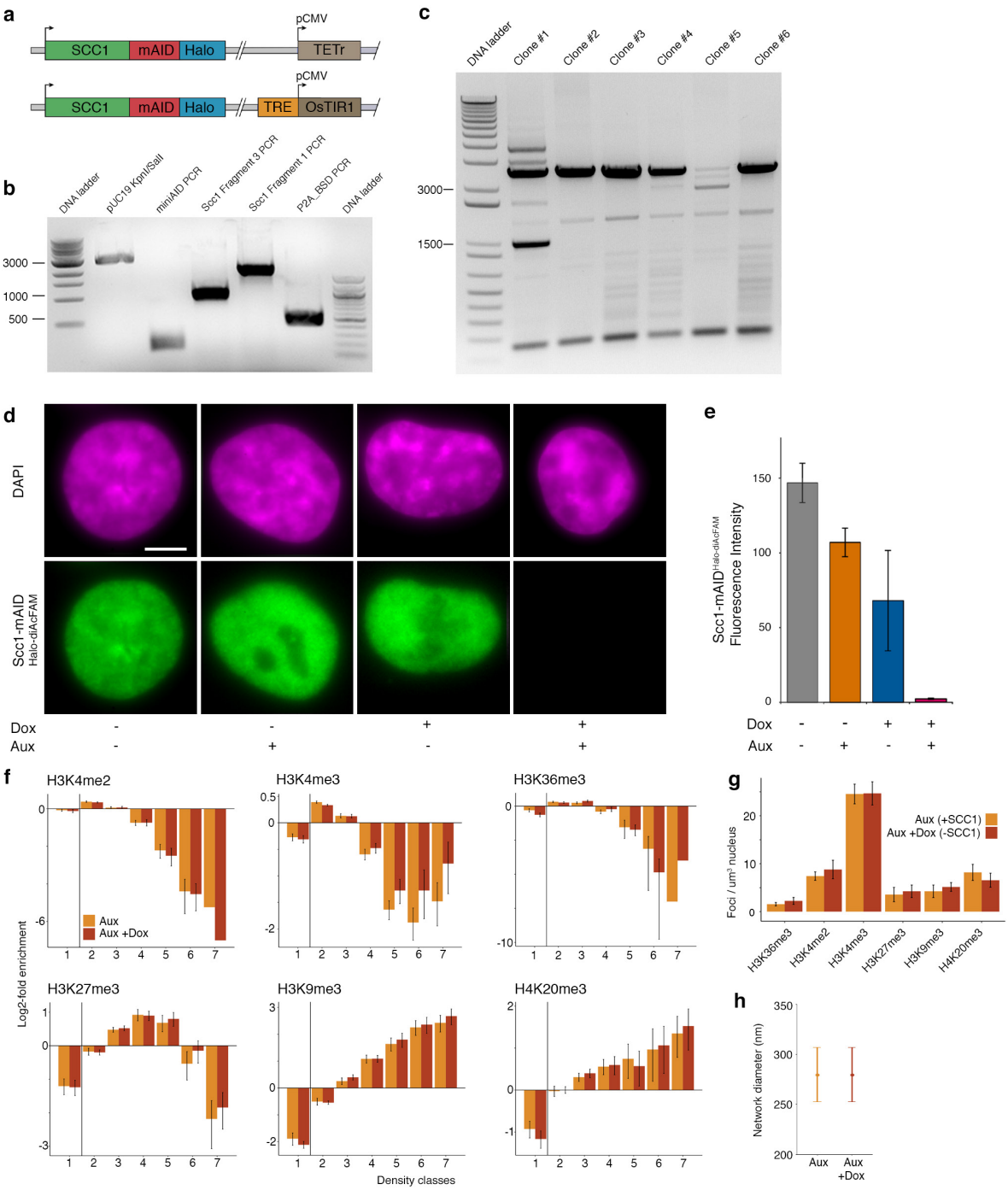

Extended Data Figure 9 | Generation of the HCT116 Tet-OsTIR1 Scc1-mAID-Halo cell line and functional marker distribution for Scc1 ablation. **a**, Schematic overview of the genomic construct. Both endogenous Scc1 alleles are tagged with an auxin-inducible degron (mAID) and a HaloTag. In the presence of doxycycline, the TIR platform is activated by the Tet system to produce an E3 ligase. The E3 ligase will induce proteosomal degradation of all mAID tagged proteins in the presence of auxin. **b**, Agarose gel of PCR amplified products required for the generation of the Scc1 CT-BSD-GSG-P2A-mAID-HaloTag construct. **c**, Screening of clones after CRISPR-Cas9 mediated incorporation of the construct described in **a** and **b**. Wildtype Scc1 has an expected size of ~1500 bp and modified Scc1 has an

767 expected size of ~3800 bp. Clone #1 shows is heterozygous for the integration whereas
768 clone #2,3,4,6 are homozygous. For this study, clone #2 was expanded. **d**, Representative
769 widefield fluorescent DAPI and SCC1-mAID signal after mock induction, 2 h auxin (aux),
770 16 h doxycycline (dox), or both 2 h aux and 16 h dox (left to right respectively). Scale bar: 5
771 *µ*m. **e**, Quantification of the fluorescent intensity in the different conditions of (d). N = 10 cells
772 per condition (error bars = SD). **f**, Bar plots of the over/under representation of each histone
773 PTM analysed in each of the segmented chromatin classes with or without Scc1 ablation (6h
774 aux +/- 16 h dox) in HCT116 cells. Plots show average log-2 value, error bars indicate 95%
775 confidence interval. **g**, Quantification of the mean number of foci detected for each condition
776 shows no significant change (error bars = SD). **h**, Quantification of the filament dimensions
777 shows no significant change between Scc1 positive or depleted conditions (bars= 95%
778 confidence interval). For analyses in **f**-**h** number of cells: Aux = 80, Aux + Dox = 104.
779

780 **Extended Data Table 1 | Average number of foci analysed per marker**

	C127			
Marker	**G1 (ΣN=433)**	**ES (ΣN=225)**	**MS (ΣN=227)**	**LS (ΣN=230)**
CTCF	7130 ± 2025 (40)	4784 ± 1699 (30)	4052 ± 2732 (30)	3878 ± 3360 (30)
H3K27me3	2590 ± 1500 (40)	1906 ± 1727 (20)	1940 ± 1734 (18)	1949 ± 1576 (20)
H3K36me2	3260 ± 1993 (20)	-	-	-
H3K36me3	1323 ± 515 (40)	2822 ± 1396 (30)	2541 ± 1153 (30)	392 ± 356 (30)
H3K4me2	2708 ± 1089 (20)	-	-	-
H3K4me3	5556 ± 1207 (40)	3692 ± 1777 (30)	2781 ± 2416 (29)	3104 ± 2778 (30)
H3K9me2	4787 ± 988 (30)	1169 ± 535 (15)	2753 ± 1405 (20)	2548 ± 1867 (20)
H3K9me3	1908 ± 1603 (30)	688 ± 230 (20)	809 ± 412 (20)	664 ± 229 (20)
H4K20me3	4523 ± 356 (20)	2598 ± 583 (20)	1959 ± 1196 (20)	2344 ± 392 (20)
H4K5ac	5177 ± 1527 (20)	-	-	-
hnRNPC1/2	4625 ± 781 (20)	1224 ± 423 (20)	865 ± 174 (20)	614 ± 220 (20)
Nascent RNA	2797 ± 1124 (13)	-	-	-
RNAPII-S2P	5027 ± 1319 (40)	2830 ± 1860 (30)	2698 ± 2530 (30)	3019 ± 2360 (30)
SAF-A	4655 ± 1821 (20)	-	-	-
Scc1	1272 ± 391 (20)	981 ± 193 (10)	991 ± 102 (10)	1146 ± 244 (10)
Smc3	615 ± 263 (20)	-	-	-

	C127			HeLa
Marker	**NaN_3 (ΣN=120)**	**Hyper-os (ΣN=120)**	**Trip (ΣN=123)**	**G1 (ΣN=41)**
CTCF	4097 ± 2491 (20)	8032 ± 1690 (20)	10717 ± 1887 (23)	-
H3K27me3	2077 ± 840 (20)	3693 ± 847 (20)	7259 ± 2978 (23)	-
H3K4me3	5814 ± 1832 (20)	5592 ± 933 (20)	8705 ± 1603 (11)	7341 ± 1785 (10)
H3K9me3	2726 ± 610 (20)	1505 ± 362 (20)	4122 ± 2250 (23)	5837 ± 525 (11)
RNAPII-S2P	6263 ± 1277 (20)	6161 ± 1157 (20)	2275 ± 900 (20)	3719 ± 819 (10)
Scc1	1272 ± 358 (20)	1046 ± 749 (20)	4971 ± 3055 (23)	-
hnRNPC1/2	-	-	-	7531 ± 1463 (10)

	HCT116 (Scc1-mAID)		IMR90	
Marker	**6hr Aux (ΣN=80)**	**6hr Aux + 16hr Dox (ΣN=104)**	**G1 (ΣN=208)**	**RS (ΣN=211)**
H3K27me3	1077 ± 516 (20)	1379 ± 407 (30)	2253 ± 418 (20)	7591 ± 3657 (19)
H3K36me2	-	-	3253 ± 2056 (20)	6416 ± 2500 (20)
H3K36me3	551 ± 138 (10)	790 ± 263 (12)	843 ± 396 (20)	2526 ± 1415 (19)
H3K4me2	2620 ± 413 (10)	3063 ± 412 (12)	4011 ± 656 (19)	6298 ± 2329 (18)
H3K4me3	7409 ± 1252 (20)	8155 ± 1420 (30)	4424 ± 555 (20)	9546 ± 5158 (20)
H3K9me2	-	-	3868 ± 628 (20)	7946 ± 2605 (20)
H3K9me3	1182 ± 204 (10)	1771 ± 174 (10)	2134 ± 490 (20)	3714 ± 2007 (19)
H4K20me3	2316 ± 387 (10)	2246 ± 272 (10)	-	-
H4K5ac	-	-	3565 ± 512 (10)	8901 ± 3504 (18)
RNAPII-S2P	-	-	3979 ± 715 (20)	7467 ± 4002 (19)
SAF-A	-	-	3823 ± 1992 (19)	11051 ± 5092 (20)
Smc3	-	-	1159 ± 287 (20)	2000 ± 1226 (19)

781

782 Average number of IF spots ± SD of each marker per cell for (N) number of cells in each
783 condition after high stringency filtering to avoid false positives. Cell cycle stages are
784 abbreviated to ES, MS and LS for earl, mid and late S phase, and RS for senescence. To
785 maintain consistency, the same mammalian antibodies were used throughout this study,
786 however the affinity of some antibodies is greater or decreased in either mouse (C127) or
787 human (HCT116, IMR90) cells. The numbers for IMR90 cells in RS are consistently at least
788 double that of G1as these are predominantly binuclear due to defective cytokinesis.
789

790 **METHODS**

791 **Plasmids**

792 pSpCas9(BB)−2A-Puro V2.0 targeting SCC1 (PX459 SCC1(Hs)) was a gift from James
793 Rhodes[50]. A poly Glycine-Serine linker, Blasticidin resistance gene (BSD), GSG-P2A, mini
794 auxin-inducible degron (mAID) and HaloTag were cloned between the KpnI and SalI site of a
795 pUC19 vector by Gibson Assembly (NEB #cat E2611). The pUC19 CT-BSD_GSG_P2A-
796 mAID-HaloTag was cloned between two 1 kb homology arms at the 3' of Scc1 to generate
797 pUC19 Scc1 CT-BSD-GSG-P2A-mAID-HaloTag.

798

799 **BACs**

800 The BACs used for FISH labelling of a single TAD were a gift from E. Heard[19]. They
801 correspond to X chromosome "TAD H" characterized between genomic loci 102325818 and
802 102998976 (673158 bp). The four BACs required to cover this region are: 6-RP24-217I10
803 (102302874:102459532), 7-RP23-469A2 (102465652:102651023), 8-RP23-331L13
804 (102648562:102834423) and 9-RP24-396M14 (102804354:102976347) spanning a total
805 length of 673473 bp. The 315bp difference between BACs coverage and TAD boundary
806 calling is considered negligible over the 673kb total (<0.05% error). BAC probes were
807 directly labelled by nick translation using CF-594 (Biotium).

808

809 **Cell culture**

810 Mouse mammary gland C127 and human cervical cancer HeLa H2B-GFP cells were grown
811 in Dulbecco's Modified Eagle Medium (DMEM) supplemented with 10% FBS, 1% penicillin
812 and streptomycin. Human colon carcinoma HCT116 Tet-OsTIR1 cells were cultivated in
813 McCoy's 5A medium supplemented with 10% FBS, 2 mM L glutamine and 1% penicillin and
814 streptomycin. Human lung fibroblast IMR-90 cells were grown in Dulbecco's Modified Eagle
815 Medium (DMEM) supplemented with 10% FBS, 1% penicillin and streptomycin. Cells were
816 incubated at 37°C, 5% CO_2 in humidified incubator. At 90% confluence cells were sub
817 cultured by trypsinising with 0.05-0.25% Trypsin in PBS or 1x trypsin replacement solution
818 (TrypLE express, Gibco) and passaged to a new culture dish at appropriate dilutions (1:5-
819 1:12 every 2-3 days).

820

821 **Generation of inducible Scc1 degradation system**

822 To generate a stable HCT116 Tet-OsTIR1 Scc1-mAID-Halo cell line, the pX459 SCC1(Hs)
823 plasmid and pUC19 Scc1 CT-BSD-GSG-P2A-mAID-HaloTag were transfected using
824 FuGene HD (Promega #cat PRE2311). Two days post transfection, cells were grown in

825 blasticidin-containing McCoy's 5A medium (5 μg/mL). After 10 days, single colonies were
826 transferred to 96-well plates and homozygous clones were screened by PCR with primers in
827 Supplementary Table 1.
828
829 **EdU, EU and BrUTP labelling and perturbation experiments**
830 To identify cells in S-phase 10 μM 5-ethenyl-deoxyuridine (EdU) was added 15-30 min
831 before fixation. G1 cells were identified by being negative for EdU pulse labelling and their
832 smaller nuclear size compared to G2 cells. Identification of G1 vs RS cells in the IMR90 cell
833 line was done using the proliferating cell marker Ki-67. G1 cells were Ki67-positve (and EdU-
834 negative) versus G2 Ki67-negative.
835 For bulk RNA labelling 1 mM EU was added 60-90 min before fixation. To label
836 nascent RNA a 10 min BrUTP pulse labelling was performed by scratch transcription
837 labelling approach as described[51].
838 For biophysical chromatin perturbation cells were incubated for 10 min before fixation
839 and immunostaining with 50 mM of NaN_3 or 200 µl of 10xPBS (to expose cells to
840 hyperosmotic conditions) added to growth medium. For transcriptional inhibition, cells were
841 incubated with 1 μM Triptolide (Sigma-Aldrich) for 90 min prior to fixation; treatment leads to
842 a strong reduction in bulk RNA signal. To Auxin induced Scc1-degradation, HCT116 cells
843 were cultivated in the presence of 5 μg/mL doxycycline (Sigma, D9891) and 500 nM auxin
844 (Sigma, cat# I5148) for 16 h and 6 h, respectively.
845
846 **RASER-FISH and probe labelling**
847 RASER-FISH maintains nuclear fine-scale structure by replacing heat denaturation with
848 exonuclease III digestion of one of the two DNA strands after UV-induced generation of
849 nicks, and is suitable for high- and super-resolution imaging analysis[34]. Briefly, cells were
850 labelled overnight with a BrdU/BrdC mix (3:1) at final conc. of 10 μM. Cells were fixed in 2%
851 formaldehyde for 15 min and permeabilised in 0.2% Triton X-100/PBS (vol/vol) for 10 min.
852 Cells were incubated with DAPI (0.5 μg/mL in PBS), exposed to 254 nm wavelength UV light
853 for 15 min, then treated with Exonuclease III (NEB) at final conc. 5 U/μL at 37°C for 15 min.
854 Labelled probes (100 ng each) were denatured in hybridization mix at 90°C for 5 min and
855 pre-annealed at 37°C for 20 min. Coverslips were hybridized with prepared probes at 42°C.
856
857 **Immunofluorescence (IF) labelling**
858 IF labelling was performed as described in detail[36,52]. The antibodies used in this
859 investigation are listed in Supplementary Table 2. One day before labelling, cells were grown

860 on 22x22 mm #1.5H high precision 170 µm ± 5 µm coverslips (Marienfeld Superior).
861 HCT116 Tet-OsTIR1 Scc1-mAID-Halo cells were fluorescently tagged by incubating with 50
862 nM HaloTag diAcFAM (Promega, cat# G8272) or 500 nM HaloTag JF488 for 30 min.
863 HCT116 cells were incubated in HaloTag-free medium for 30 min to remove residual ligand.
864 Prior to fixation, cells were washed twice with PBS. Cells were fixed in 2%
865 formaldehyde/PBS (Sigma, #cat F8775) for 10 min, washed with 0.02% Tween-20/PBS
866 (PBST) and permeabilized in 0.1-0.5% Triton-X-100/PBS. Coverslips were washed three
867 times with PBST and incubated for 30 min in MaxBlock (Active motif, cat# 15252). Cells
868 were stained with primary antibodies against the protein of interest, washed three times with
869 PBST and stained with fluorescently labelled secondary antibodies. After washing, cells
870 were post-fixed in 4% formaldehyde/PBS for 10 min and counterstained using 1-2 mg/μL
871 4',6-diamidino-2-phenylindole (DAPI) for 10 min. Coverslips were mounted in non-hardening
872 Vectashield (Vector Laboratories, cat# H-1000) and stored at 4°C.
873
874 **Super-resolution image acquisition, reconstruction and quality control**
875 3D-SIM images were acquired with a DeltaVision OMX V3 Blaze system (GE Healthcare)
876 equipped with a 60x/1.42 NA PlanApo oil immersion objective (Olympus), pco.edge 5.5
877 sCMOS cameras (PCO) and 405, 488, 593 and 640 nm lasers. For fixed cell imaging, 3D
878 image stacks were acquired over the whole cell volume in z and with 15 raw images per
879 plane (five phases, three angles). Spherical aberration was minimized using immersion oil
880 with RI 1.514 for sample acquisition. The raw data was computationally reconstructed with
881 SoftWoRx 6.5.2 (GE Healthcare) using channel-specific OTFs recorded using immersion oil
882 with RI 1.512, and Wiener filter settings between 0.002-0.006 to generate 3D stacks of 115
883 nm (488 nm) or 130 nm (592 nm) lateral and approximately 350 nm axial resolution. All SIM
884 data was routinely and meticulously quality controlled for effective resolution and absence of
885 artifacts using SIMcheck[53], an open-source Image J plugin to assess SIM image quality via
886 modulation contrast-to-noise ratio, spherical aberration mismatch, reconstructed Fourier plot
887 and reconstructed intensity histogram values. (for more details see [52]). Multi-channel
888 acquisitions were aligned in 3D using Chromagnon software[54] based 3D-SIM acquisitions of
889 multi-colour EdU labelled C127 cells[36]. 3D-SIM imaging of DAPI or SYTOX Green stained
890 DNA typically provides a high-contrasted spatial representation of chromatin distribution with
891 a lateral resolution of down to 100-115 nm (Extended Data Fig. 1a).
892 For live cell 3D-SIM, HeLa H2B-GFP cells were seeded in a 35 mm μ-Dish, high
893 Glass Bottom (Ibidi) using phenol red free DMEM medium supplemented with 10 μM
894 HEPES. Live cell imaging was performed at 5% CO_2 supply and keeping sample at 37°C

895 using stage and objective heater) we recorded for each timepoint a central region over 7 z-
896 positions with 125 nm distance covering a total range of 0.75 μm and totalling 105 raw
897 images (5 phases x 3 angles x 7 z-positions). Using 10 ms exposure time and 31% laser
898 transmission of the 488 nm laser a frame rate of down to 0.5 Hz could be achieved, and
899 typically 12 to 18 time points could be recorded until the photon budget was exhausted due
900 to photobleaching. The reconstructed z-sections were processed in Fiji applying a maximum
901 intensity z-projection followed by *Bleach Correction* (histogram matching) and *Linear Stack*
902 *Alignment with SWIFT* (affine transformation) to compensate for photobleaching and nuclear
903 motion/deformation.
904 3D STED micrographs of SYTOX green stained C127 cells were acquired on a Leica
905 TCS SP8 STED 3X system equipped with a 100x/1.4 NA oil objective using 50% of depletion
906 energy for axial resolution increase resulting in a nominal resolution of ~100 nm in x-y and
907 ~200 nm in z-direction. To compensate for low dynamic range and SNR raw STED data was
908 subjected to a constrained iterative 3D deconvolution using Huygens software (SVI). 3D
909 STED achieves comparable or slightly better resolution than 3D-SIM for high labelling
910 density samples such as chromatin at the expense of slower acquisition speed, a major
911 drawback in a high-throughput analysis investigation.
912
913 **Quality validation**
914 3D-SIM imaging and subsequent quantitative analyses is susceptible to artefacts[52]. For
915 instance, bulk labelling of densely packed chromatin inside mammalian nuclei of several μm
916 depth entails high-levels of out-of-focus blur, which reduces the contrast of illumination stripe
917 modulation and thus the ability to recover high frequency (i.e., super-resolution) structure
918 information. We therefore carefully assessed and optimized system performance as well as
919 raw and reconstructed data quality using SIMcheck ImageJ plugin[53] (Extended Data Fig. 1a).
920 To exclude potential false positive calls, we used the *Modulation Contrast-to-Noise-Ratio*
921 *(MCNR) map* macro of SIMcheck, which generates a metric of local stripe contrast in
922 different regions of the raw data and directly correlates with the level of high-frequency
923 information content in the reconstructed data[52]. Only IF spot signals whose underlying
924 MCNR values exceed a stringent quality threshold were considered while localisations with
925 low underlying MCNR were discarded to exclude any SIM signal which falls below
926 reconstruction confidence in all datasets before feeding these to the analysis pipeline
927 (Supplementary Fig. 1). We noted that most nuclear spots (dependent on the antibody
928 between a few hundred to several thousand per nucleus) were in the size range of 3D-SIM
929 resolution limited point signal, and their intensities were similar to seldom extranuclear spots

930 from non-specifically bound primary-secondary antibody complexes (concentrating less than
931 10 dyes). We therefore conclude that nuclear signals predominantly represent the binding of
932 a primary-secondary antibody complex to a single epitope.
933
934 **Cha*i*N - pipeline for high-content analysis of the 3D epigenome**
935 Cha*i*N (for Chain high-throughput analysis of the *in situ* Nucleome) describes a pipeline of
936 scripts for the automated high-throughput analyses in this investigation (Extended Data Fig.
937 5). In brief, the counterstain/chromatin channel is used to generate (1) a nuclear mask and
938 (2) segment chromatin topology into 7 intensity/density classes using an R script that is
939 expanding on a Hidden Markov model[55]. Based on the output of Cha*i*N, we can
940 quantitatively assess multiple parameters, such as the overall volume of the chromatin
941 filament (combined classes 2-7, Extended Data Fig. 1d, e) versus IC (class 1), its 3D
942 surface, and the surface-to-volume-ratio. The volume of the segmented chromatin fraction
943 occupied approximately two thirds of the total nuclear volume (~400 of 600 μm^3 in G1 C127
944 cells).
945 The IF signals for markers are thresholded by intensity using the Otsu algorithm, with
946 all non-foci voxels replaced by zeros. The complement of this is image is segmented by a 3D
947 watershed algorithm and the 3D centroid coordinates extracted from each segmented
948 region's centre of mass after weighting by local pixel intensities. To filter out potential false
949 positive localizations using a local modulation-contrast-to-noise-ratio (MCNR) threshold to
950 avoid potential artefacts skewing the statistical output[52,53] (Supplementary Fig. 1). The
951 quality controlled and filtered centroid positions were then related to the chromatin-
952 interchromatin volume in two ways: The spot positions falling into each of the 7 segmented
953 classes were counted, normalized to the respective class size and their relative enrichment
954 (or depletion) displayed in a heat map on a log 2-fold scale.
955 Indexing IF coordinates on the segmented chromatin yields their
956 enrichment/depletion profiles at different chromatin densities normalized to the volumes of
957 each chromatin density class. Segmentation of the 3D surface between class 1 and all other
958 classes allows for Euclidian distance calculation between the IF coordinates and the nearest
959 filament surface voxel. The segmented surface can also be normalized to the volume of total
960 chromatin to obtain a surface area to volume ratio of the filament.
961 Finally, by sampling the distance between the surface and random coordinates,
962 assuming a tubular based structure, it is possible to estimate the average radius and
963 diameter of the filament (Extended Data Fig. 3). The average radius R can be sub divided
964 into a smaller radius "r" which encompasses the inner half of the volume of the tube (and

965 therefore half the area of the cross-section) and δ, the difference between r and R. First, we
966 define two circles (A1 with radius r+δ and A2 with radius r) of which the area of A1 is twice
967 the area of A2. Based on simple calculus we can determine that R = 3.4142 δ. Second, if we
968 randomly distribute points over the entire tube, 50% of the points will be located within circle
969 A2 whereas the other 50% will located in A2 - A1. Third, if we calculate the minimum
970 distance of the points in the circle of A2 - A1 we can define the value of δ, which is 50% of
971 the area under the frequency curve of the right histogram. Lastly, by multiplying this value
972 with 3.4142, we can estimate the average radius of tubular chromatin filaments in cell nuclei.
973 We note, the total number of discrete segmentation bins used in this analysis is arbitrary,
974 with the sole criterion to group all non-detectable chromatin voxels as one class (class 1, IC).
975 It is therefore an important validation of this approach to observe that, on average,
976 elongating RNAP (RNAPII-S2P) primarily localizes at the chromatin-IC interface or within +/-
977 20 nm of this feature with 95% confidence, suggesting that the *in silico* determined boundary
978 between IC or chromatin in this analysis is true to an underlying biological demarcation.
979
980 **Quantitative evaluation of chromatin dynamics**
981 Spatial correlation dynamics of chromatin was estimated by using Dense Flow
982 reConstruction and Correlation (DFCC)[31]. Briefly, DFCC was applied to estimate the 2D
983 apparent motion of two consecutive images in an image sequence (N-1); the direction and
984 magnitude of flow fields of each pixel (size = 41 nm) were estimated for H2B-GFP over 20
985 image series and with time interval of 2 s. Then, spatial auto-correlation of scalar fields
986 representing motion direction was calculated by Fast Fourier Transform algorithms and is
987 given by

$$r(\Delta x, \Delta y) = \frac{\mathcal{F}^{-1}[\mathcal{F}(\gamma) \cdot \mathcal{F}^{*}(\gamma)]}{\langle\gamma\rangle\langle\gamma\rangle},$$

988 where $\mathcal{F}(\cdot)$, $\mathcal{F}^{-1}(\cdot)$, and $\mathcal{F}^{*}(\cdot)$ are the Fourier transformation, inverse Fourier transformation
989 and the complex conjugate of the Fourier transformation, respectively. Correlation corves for
990 different time lags were fitted using the Whittle-Màtern model, and therefore, the correlation
991 length and smoothness parameters extracted for each time lags.
992 Hi-D method was applied to estimate the biophysical properties of chromatin motion
993 in living Hela cells at pixel resolution (41 nm)[49].
994 Mean square displacement (MSD) curves were plotted over time lags representing
995 the trajectories of chromatin in the entire nucleus. Then, Bayesian inference approach
996 applied to test the below five principle models for each MSD curves in order to classify types
997 of motion. Fitting of the MSD derived from trajectories can be expressed for anomalous

diffusion (α), free diffusion constant (D), directed motion (V) or a combination thereof. The value of each biophysical parameter extracted by this fitting is then mapped in 2D colour map, also five principal models are shown as a coloured map directly on the nucleus (Extended Data Fig. 2b).

$$MSD_D(\tau) = 4D\tau + o$$

$$MSD_{DA}(\tau) = 4D\tau^{\alpha} + o$$

$$MSD_V(\tau) = v^2\tau^2 + o$$

$$MSD_{DV}(\tau) = 4D\tau + v^2\tau^2 + o$$

$$MSD_{DAV}(\tau) = 4D\tau^{\alpha} + v^2\tau^2 + o$$

Where D: Free diffusion; DA: Anomalous diffusion; V: Drift velocity of flow fields; DV: Free diffusion + drift; DAV Anomalous diffusion + drift; τ: Time interval.

Data and Code Availability

All data, parameters and scripts used are available for reproducing the results of this investigation. Raw and reconstructed 3D SIM images, with reconstruction and alignment parameters will be made publicly available at the Image Data Resource (IDR). The programs required to run all scripts for image analysis are: ImageJ (Fiji distribution with SIMcheck), R and Octave. Scripts for ChaiN and the DFCC analysis are available in the following GitHub repositories: https://github.com/ezemiron/Chain, https://github.com/romanbarth/DFCC.